Plasma synthetic jet actuators for active flow control

Zong, Haohua; Chiatto, Matteo; Kotsonis, Marios; de Luca, Luigi

DOI
10.3390/act7040077

Publication date
2018

Document Version
Final published version

Published in
High-Throughput

actuators

MDPI

Review

Plasma Synthetic Jet Actuators for Active Flow Control

Haohua Zong [1,*], Matteo Chiatto [2], Marios Kotsonis [1] and Luigi de Luca [2]

[1] Faculty of Aerospace Engineering, Delft University of Technology, 2629 HS Delft, The Netherlands; M.Kotsonis@tudelft.nl

[2] Department of Industrial Engineering, Aerospace Sector, Universitá degli Studi di Napoli "Federico II", p.le Tecchio 80, 80125 Naples, Italy; matteo.chiatto@unina.it (M.C.); deluca@unina.it (L.d.L.)

* Correspondence: H.Zong-1@tudelft.nl

Received: 31 August 2018; Accepted: 28 October 2018; Published: 1 November 2018

Abstract: The plasma synthetic jet actuator (PSJA), also named as sparkjet actuator, is a special type of zero-net mass flux actuator, driven thermodynamically by pulsed arc/spark discharge. Compared to widely investigated mechanical synthetic jet actuators driven by vibrating diaphragms or oscillating pistons, PSJAs exhibit the unique capability of producing high-velocity (>300 m/s) pulsed jets at high frequency (>5 kHz), thus tailored for high-Reynolds-number high-speed flow control in aerospace engineering. This paper reviews the development of PSJA in the last 15 years, covering the major achievements in the actuator working physics (i.e., characterization in quiescent air) as well as flow control applications (i.e., interaction with external crossflow). Based on the extensive non-dimensional laws obtained in characterization studies, it becomes feasible to design an actuator under several performance constraints, based on first-principles. The peak jet velocity produced by this type of actuator scales approximately with the cubic root of the non-dimensional energy deposition, and the scaling factor is determined by the electro-mechanical efficiency of the actuator (O(0.1%–1%)). To boost the electro-mechanical efficiency, the energy losses in the gas heating phase and thermodynamic cycle process should be minimized by careful design of the discharge circuitry as well as the actuator geometry. Moreover, the limit working frequency of the actuator is set by the Helmholtz natural resonance frequency of the actuator cavity, which can be tuned by the cavity volume, exit orifice area and exit nozzle length. In contrast to the fruitful characterization studies, the application studies of PSJAs have progressed relatively slower, not only due to the inherent difficulties of performing advanced numerical simulations/measurements in high-Reynolds-number high-speed flow, but also related to the complexity of designing a reliable discharge circuit that can feed multiple actuators at high repetition rate. Notwithstanding these limitations, results from existing investigations are already sufficient to demonstrate the authority of plasma synthetic jets in shock wave boundary layer interaction control, jet noise mitigation and airfoil trailing-edge flow separation.

Keywords: plasma; synthetic jet; actuators; flow control

1. Introduction

Active flow control (AFC), serving as one of the most popular research topics in fluid dynamics, mainly refers to the process of favourably modifying the natural behaviour of a flow field via controllable devices (actuators) [1]. An efficient flow control system, can not only improve the energy efficiency of transportation vehicles (e.g., reducing the fuel consumption), but also benefit many industrial processes involving fluid flows (e.g., fuel-gas mixing enhancement, jet noise mitigation) [2,3]. Nowadays, a large amount of flow control methods are available for both external boundary layers and

internal flows, and the selection of a specific control method mainly depends on the particular goal to be achieved. In the last 15 years, plasma synthetic jet actuators (PSJAs), or sparkjets, have drawn significant attention from the active flow control community, due to their ability to produce high velocity (>300 m/s) pulsed jets at high frequency (>5 kHz), thus promising to be applied in high-Reynolds number (i.e., $O(10^6 - 10^7)$) practical flows (e.g., aircraft wings, inlets, helicopter blades).

A PSJA is an electromechanical device, typically composed of two or three electrodes embedded in a small cavity linked to the external environment through an exit orifice. A complete working cycle begins with an electrical discharge between the electrodes, which sharply elevates the pressure and temperature of the actuator cavity via arc heating. Subsequently, the high-pressure air is expelled through the orifice, converting the enthalpy of cavity air into jet kinetic energy. Following the jet expulsion, fresh air is drawn back inside the cavity, mixing with the residual high-temperature low-density and awaiting the next pulse. After dozens of cycles, the device reaches a steady working stage characterized by the periodical variations of exit velocity, density and temperature, thus producing zero-net mass flux jets, i.e., plasma synthetic jets (PSJs).

Notwithstanding the time-averaged mass flux in one cycle is null, a non-zero time-averaged momentum flux is imparted to the external environment by the actuator. Since the jet is synthesized directly from the surrounding fluid, no continuous fluid supply is required, which largely mitigates the weight and volume penalty incurred by the external compressors or vacuum pumps in conventional fluidic flow control methods (e.g., steady jets, suction) [4,5]. Similar to the surface dielectric discharge actuators (SDBDAs), the operation of PSJAs is purely electrical and involves no mechanical components, resulting in a rapid response (O(μs)) and high bandwidth (O(10 kHz)). As a comparison to other mechanically driven synthetic jet actuators (based on piezoelectric elements, loudspeakers, pistons and others), PSJAs are able to produce a jet with much higher velocity, without the aid of any moving parts, thus eligible for flow control in the transonic and supersonic regimes. One of its disadvantage is related to the high temperatures reached within the cavity and the electromagnetic fields induced by the operating device, which can lead to integration issues with the surrounding structures, as described in Section 2.4.

PSJAs were first developed in 2003 by Johns Hopkins University (JHU) [6]. In its earliest version, the device was composed of three electrodes including an anode, a sharp cathode and a grid, all of which are embedded in a ceramic body. A weak cathode-to-grid discharge was used to trigger the device, while the main discharge occurred between the cathode and anode. An updated version of these devices was presented one year later [7,8], with the grid electrode removed and the electrical discharge directly generated between the anode and cathode. These adjustments enabled a higher robustness, a simpler structure, and a greater flexibility in testing. Nevertheless, as another consequence of the removal of the external trigger, the discharge energy in the updated version becomes dependent on the breakdown voltage of air gap, inconveniencing the tuning of issued jet intensity. As such, the natural evolution of the actuators went towards the three-electrodes configuration, with a ground electrode, a main electrode and a trigger one. In this case, the discharge occurs only when the trigger voltage is activated (O(kV)), ionizing the air electrode gap and allowing the capacitor energy to be released between the main electrodes (few hundreds volts discharge) [9]. Nowadays, the power supply system has moved from an external trigger to a pseudo-series trigger [10]. Namely, the third trigger electrode has been removed, and both the trigger and main discharge are integrated into the anode. The simplified configuration allows a much larger electrode gap because the trigger discharge spans the whole electrode gap. Further details can be found in Section 2.2.

Few years later after the proposal of PSJAs by JHU, several other research groups stepped into the field, which considerably promoted the development of PSJAs. Of all these contributions, the efforts made by ONERA (French Aerospace Lab) and the University of Toulouse (France) worth special mention. They studied the PSJ device in quiescent and cross-flow condition both numerically and experimentally [11,12]. Two discharge circuits (capacitive vs. inductive) were devised, and the effect of energy deposition stage on the evolution of main thermodynamic and electrical quantities

of the device were focused [13,14]. Based on these experimental data, a numerical model was calibrated and validated, allowing the simulation of detailed jet evolution in different cases [15,16]. Subsequently, the University of Texas at Austin (USA) [17,18] analysed the effectiveness of PSJs in shock wave/boundary layer interaction control, and the Rutgers University (USA) and the University of Illinois at Urbana-Champaign (USA) [19,20] examined the characteristics of PSJAs in quiescent conditions from both numerical and experimental perspectives. At the time, other groups were also known for their works on this topic: Air Force Engineering University (China), Xi'an Jiaotong University (China) [21], Delft University of Technology (The Netherlands) [22] and University of Naples (Italy) [23]. All of these groups were focused on the device characterization. At the moment, this technology seems ready to move towards flow control problems.

This paper provides a timely review of the development of PSJ technology in several aspects, ranging from the formation and evolution of PSJs in quiescent air and crossflow boundary layer, to the flow control applications of PSJAs at moderate to high-Reynolds number conditions. The content is organized as follows. Section 2 concerns the basic working principles of the actuator and power supply system, as well as several practical issues related to actuator construction (i.e., materials) and integration (i.e., electromagnetic interference). Section 3 is dedicated to the characterization of PSJAs in quiescent flow, and three subsections are included, respectively corresponding to the present achievements in experiments, numerical simulations and low-order analytical models. A separate efficiency analysis is performed later on in Section 4, and the flow control applications of PSJAs at moderate- to high-Reynolds number are summarized in Section 5.

2. Plasma Synthetic Jet Actuator System

This section prepares the knowledge necessary for producing PSJs. The basic working principles of the actuator is introduced in Section 2.1, followed by a detailed description of the different concepts of the power supply system in Section 2.2. In Sections 2.3 and 2.4, the effects of actuator material and electromagnetic interference are further discussed .

2.1. Working Principles

The operation process of the actuator involves complex energy conversion across multiple disciplines, i.e., electrical engineering, gas discharge, plasma heating, thermodynamics and gas dynamics. During simplified analysis, a complete working cycle is typically divided into three stages: energy deposition stage, jet stage, and refresh stage. Note that this division, in some cases, can betray reality. For example, under conditions of long discharge duration (O(100 μs)) and low repetition rate, the energy deposition stage and jet stage would happen simultaneously, meanwhile multiple alternations between the jet and refresh stages are perceived (see Figure 1). Figure 2 shows a sketch of the three working stages. Accompanying the sketch, detailed interpretations of a complete working cycle are provided as follows:

- The cycle begins with the generation of an electrical arc/spark within the cavity which provides energy to the fluid and quickly increases its temperature and pressure. Since the energy discharge is locally confined between the electrode gap, the spatial distributions of temperature and pressure are non-uniform. Several shock waves are produced, moving outwards at supersonic speed [24]. Details on the energy deposition process are reported in Section 2.2.
- After the energy deposition, the high-pressure air is exhausted through the orifice/slot, converting the internal energy of the cavity air into jet kinetic energy. During this process, a vortex ring forms near the orifice exit and convects downstream towards the far field under self-induction. The cavity pressure decreases due to the jet expulsion and the heat transfer through the actuator cavity wall. The jet evolution process depends on both the electrical parameters (e.g., the amount of energy transferred to the cavity air, the discharge duration) [25], and the geometric quantities of the actuator (e.g., exit orifice area, throat length, cavity volume, electrode distance and location) [26] .

- The jet stage terminates with a negative differential pressure across the exit throat [27], which drives the air into the actuator cavity and initializes the refresh stage. The ingested low-temperature ambient air is subsequently mixed with the high-temperature cavity air, thus resetting the actuator cavity to its original state. Additionally, the convective and radiative heat transfer between the cavity and external environment also benefit the actuator recovery.

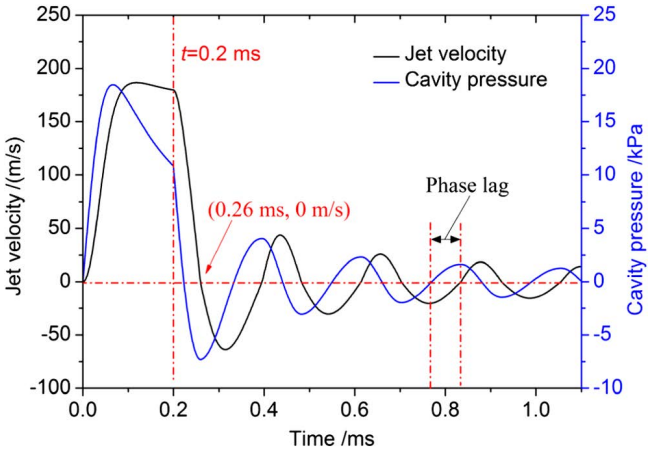

Figure 1. Evolutions of jet velocity and cavity pressure [28].

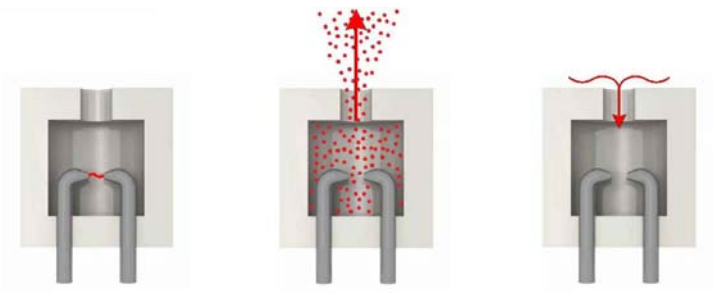

Figure 2. Different phases in one working cycle of plasma synthetic jet (PSJ).

In contrast with the conventional mechanically driven synthetic jets where the periodical alternation of ejection and suction phases is caused by the time-varying cavity volume, the cavity pressure oscillation in the case of PSJAs is driven by the periodical energy deposition of pulsed arc discharge. Another difference between these two types of synthetic jet actuators (SJAs) lies in the fact that, regardless of the actuation frequency, PSJAs can always exhibit a natural frequency in the exit velocity curve, i.e., the Helmholtz natural oscillation frequency. This aspect will further be elaborated in Section 3.3.3.

For 'synthesizing' a turbulent jet eventually convecting 'steadily' downstream, a few working cycles are necessary to create a train of vortex rings that interact with each other. During the suction phase of mutual interaction, a stagnation point is formed, at about one orifice diameter away from the exit orifice. This point separates the near-field where the flow is directed towards the cavity, from the far field where a high-speed jet prevails.

2.2. Power Supply Systems

The power supply system plays a fundamental role for producing powerful PSJs. As a prerequisite for discharge ignition, the power supply should deliver a peak voltage higher than the breakdown voltage of the present electrode gap [29]. Typically, a low-voltage DC power supply, an electrical switch (e.g., a transistor), a high-voltage transformer and several other electrical components are combined, e.g., in a flyback configuration, to generate high-voltage pulses with low costs, rather than directly using a high-voltage DC power supply [13]. Subsequently, an energy-storing capacitor is used to store the discharge energy a priori, and its voltage increases monotonically during capacitor charging. Once the breakdown voltage of the electrode gap is exceeded, a strong arc is initiated, and the electrical energy is released rapidly (O(10 µs)) as gas heating energy.

Notwithstanding the cheap construction, the above discharge configuration presents a noticeable limitation in the adjustment of discharging energy. Specifically, the discharge energy is proportional to the square of the breakdown voltage of the electrode gap which can fluctuate significantly due to the oxidation and degradation of electrode tips, as well as the variation in mean cavity pressure [9]. This fluctuation in breakdown voltage lowers the synchronization accuracy between discharge and diagnostic systems, imposing significant measurement uncertainties during experimental investigations. The introduction of a trigger function allows an easy synchronization, and an overall improvement of the reproducibility and reliability of the experiments. This trigger function, in its earliest realizations, demanded the addition of a third electrode (trigger electrode). However, in later developments, the trigger function is integrated into the anode, resulting in a two-electrode configuration operating in the so-called pseudo-series mode [30].

Nowadays, the majority of the power supply systems consist of a high-voltage *trigger circuit* and a low-voltage (*sustain circuit*), as depicted in Figure 3. The working principles of both circuits are described hereafter [28,31]:

- The *trigger circuit* is mainly composed of an internal DC power supply, a flyback circuit and a trigger transformer. The DC power supply provides a low adjustable voltage, which, through the flyback converter, is led to values of O(100) V. When switched on, the capacitors inside the circuit begin to discharge across the trigger transformer (with a ratio around 1:30) that quickly (in a few µs) raise the voltage between the electrodes.
- The *sustain circuit* is represented by an external DC power supply, whose discharge time is controlled by a MOSFET (metal-oxide-semiconductor field-effect transistor), a 'mixer' consisting of two diodes, and an electrical ballast. The power supply can provide a voltage of up to O(500) V, which by itself is not able to produce a spark between the electrodes. The 'mixer' combines the electrical outputs of the trigger and sustain circuits together, while the electrical ballast protects the system.

The trigger spark initializes the arc discharge by momentarily establishing a discharge channel between the two electrodes. As such, the actuation frequency is fully determined by the trigger frequency, while the amount of discharge energy provided to the fluid in each cycle depends on both the switch-on time of the MOSFET and the discharge current in the sustain circuit. Adjustment of the discharge current is realized by varying either the sustain voltage of the low-voltage DC power supply, or the current-limiting resistance between the mixer and actuator.

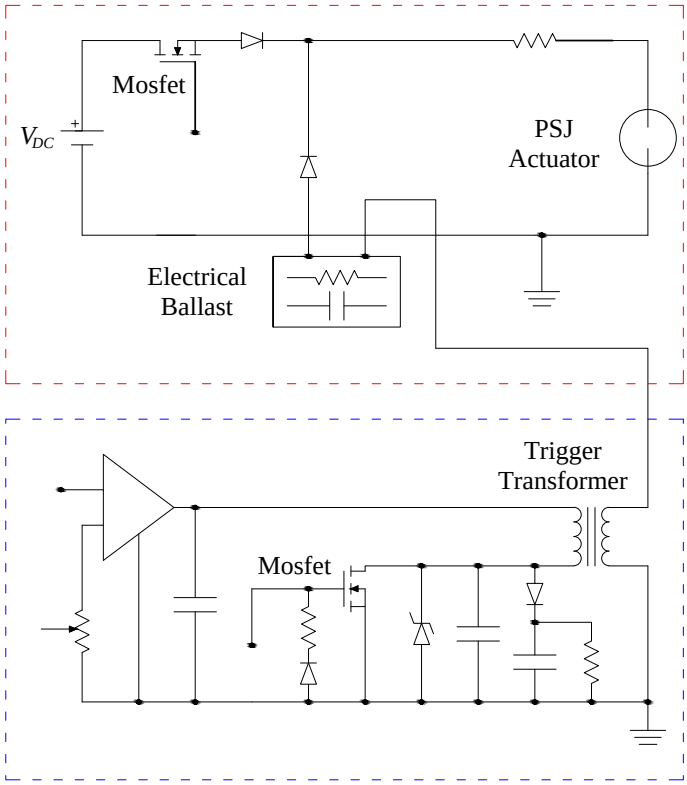

Figure 3. Power supply system: the sustain circuit (top) and the trigger circuit (bottom) [31].

2.3. Actuator Construction

So far, various PSJAs with different shapes, sizes and electrode configurations have been designed. Typically, the actuator consists of a semi-enclosed cavity housing the electrodes and a top cap with an exit orifice. These two components are fitted together via step grooves or threads. The actuator cavity is usually made of insulating materials including Teflon and machinable glass ceramic (MACOR) for high-voltage isolation purposes, whereas the actuator caps can be either insulating or metallic depending on the electrode location (brass [32], copper [33], steel [34], Macor [23]).

Due to the high temperature reached within the cavity, tungsten electrodes are widely employed. Their dimensions and shapes can influence not only the device efficiency, but also the discharge stability (e.g., occurence of misfires). A first investigation on the influence of electrodes shape and size was carried out by Haack et al. in [10], where electrodes with two different tip shapes (cylindrical and truncated cone) are tested in pure tungsten and tungsten alloys (lanthanated, ceriated, zirconated and a copper/tungsten alloy known as Elkonite). They found out that the cylindrical tip shape for both electrodes (anode and cathode) produced the best actuator performance with a low misfire percentage, which can be attributed to the relatively higher electric field at its corners. For all the materials tested, only copper/tungsten electrodes did not exhibit a good survivability, largely because the addition of copper incurred a significant alteration of the tip shape which lead to noticeable misfires in several burst sequences. Moreover, Haack et al. [10] also studied how the electrode diameter can affect the frequency response of the actuator, when the same material and tip shape were used. Results indicated that the cut-off frequency increases monotonically with the electrode length-to-diameter ratio. With a length-to-diameter ratio above 24, a cut-off frequency higher than 1 kHz can be obtained.

2.4. Electromagnetic Interference

Due to the electromagnetic compatibility (EMC) issues arising from the high-voltage (O (10 kV)) high-current (O (100 A)) arc discharge, the integration of the PSJA system underneath the skin of an aerodynamic surface (e.g., in the case of airfoil separation control) can be challenging. The actuators could electromagnetically interfere with the operation of other surrounding electronic devices (e.g., autopilot/auto-throttle computer, flight data recorder sensors, flight control system), producing unexpected or even hazardous behaviours.

Arena et al. [35] considered the potential installation of PSJAs on the upper skin of a morphing flap. A simplified test article is designed to support all experimental activities, which can be a fair representation of the actual PSJ-skin assembly. Experimental measurements showed that after appropriate shielding the electric field produced by the device seems to be compatible with the typical devices mounted within the morphing flap, and the magnetic field under all the tested conditions was always negligible. Through this preliminary experimental investigation, Arena et al. came up with a safety-critical area for the installation of flap electric actuation, control drivers and sensing network.

3. Characterization in Quiescent Flow

This section deals with the characterization of PSJAs in quiescent flow, focusing not only on the experimental and numerical investigations, but also on the reduced-order analytical models developed to predict the temporal evolution of the main quantities inside the cavity as well as at the orifice (e.g., cavity temperature/density, jet exit velocity/density).

3.1. Experimental Studies

This section explores the experimental characteristics of PSJs in quiescent conditions. Both formation and evolution processes of the plasma synthetic jets are considered and they are clearly distinguished by the venue, i.e., inside or outside the cavity. As shown in the top row of Figure 4, the term *formation* of PSJs refers to a process in which the total enthalpy of the cavity gas is suddenly elevated through the arc discharge and further transformed into the mechanical energy of the expelled gas. The input to the formation process is a time-varying discharge waveform determined by the coupling between the external discharge circuitry and the arc plasma, while the output is a zero-net mass flux jet. The goal of formation studies is to reveal the complex transfer function between input (electrical) and output (mechanical) parameters (e.g., $P_d(t) \rightarrow U_e(t)$). Such characterization involves multiple disciplines, including electrical engineering, gas discharge and plasma physics, as well as fluid dynamics. Following the characterization of PSJ formation, the term *evolution* of PSJs refers to the process in which a slug of low-density, high-temperature fluid is abruptly released to the surroundings via an exit orifice and subsequently drawn back [4]. The links between formation and evolution processes are the jet exit parameters (i.e., time-varying exit velocity, pressure and density). Once these parameters are set, the developing jets can be fully predicted by the Navier–Stokes equations, as shown in the bottom-right of Figure 4.

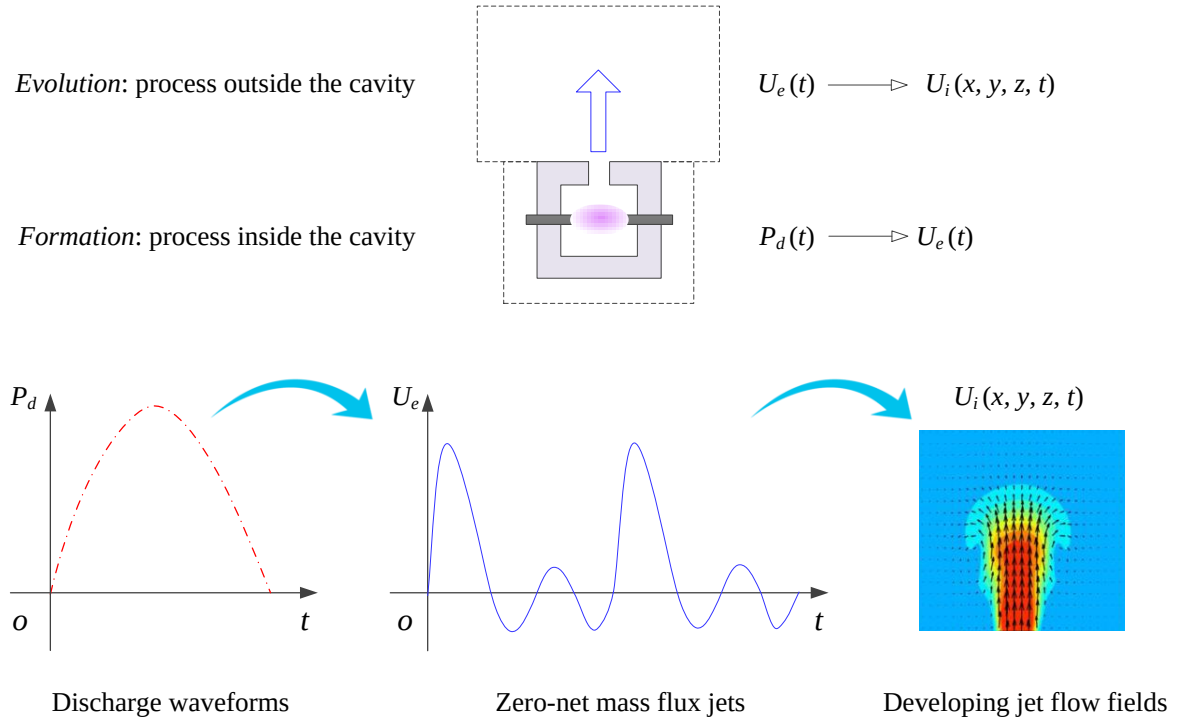

Figure 4. Sketch of formation (inside the cavity) and evolution (outside the cavity) process of plasma synthetic jets. P_d and U_e are the discharge power and the time-varying exit velocity, respectively. $U_i(x, y, z, t)$ $(i = x,\ y,\ z)$ denotes the instantaneous velocity field of developing jets.

3.1.1. Jet Formation Parameters and Jet Intensity Metrics

The parameters influencing the performance of PSJ actuators in quiescent flow are termed as jet formation parameters, which can be classified into three categories, i.e., electrical, geometrical and atmospheric. For each jet formation parameter, the relevant investigations (sorted by date of publication), as well as the diverse experimental techniques adopted in these studies including Particle Imaging Velocimetry (PIV), Schlieren imaging (SI), total pressure probes (TPPs), miniature thrust test bed (MTTB) and pendulum apparatus (PA) are listed in Table 1. Prior to reviewing the outcomes of these studies, it is necessary to discuss the jet performance metrics that can be accessed by different measurement techniques.

The simplest approach to quantify the intensity of pulsed jets is to use a total pressure probe, which delivers the jet total pressure ($\bar{P}_t$) at some distance (typically 1–2 D) away from the exit orifice [13,23,34,36]. For fully expanded nozzle flow, the following relationship holds,

$$P_t = P_s(1 + \frac{\gamma - 1}{2} M_{jet}^2)^{\frac{\gamma}{\gamma - 1}} \tag{1}$$

where, P_s is the ambient pressure; M_{jet} is the local jet Mach number defined as $U_{jet}/\sqrt{(\gamma R T_{jet})}$. T_{jet} and U_{jet} represent the time-varying temperature and velocity at the measurement location, respectively. U_{jet} must be distinguished from the spatially averaged jet exit velocity (U_e) defined in [33]. Only if the diameter of the TPP is sufficiently small with respect to the orifice diameter and its location is close enough to the exit orifice, U_{jet} can be replaced by U_e.

In the case that a dynamic pressure transducer with sufficient bandwidth is hosted inside the total pressure probe, the time-varying jet total pressure as well as the peak jet Mach number can be resolved [13]. However, care should be taken to correct possible amplitude and phase deviations, governing dynamic pressures in thin tubes, as well as avoiding resonance effects. In contrast, for the probe connected with a static pressure transducer via long tubes, only the time-averaged jet total

pressure ($\bar{P}_t$) is obtained. In a low-velocity regime ($Ma_{jet} < 0.3$), $\bar{P}_t$ can be expressed explicitly as Equation (2) [34], where f_d and T_d denote the repetition rate and cycle period, respectively.

$$\bar{P}_t = f_d \int_0^{T_d} [p_s + 0.5 \cdot \rho_{jet}(t) U_{jet}^2(t)] \cdot dt \quad (2)$$

Table 1. Classification of previous studies based on the investigated jet formation parameters and the experimental techniques used. MTTB—miniature thrust test bed; DPT—dynamic pressure transducer; SI—schlieren imaging; TPP—total pressure probe; PIV—particle imaging velocimetry; PA—pendulum apparatus.

Category	Parameters	Referenced Studies	Measurement Techniques
Electrical	Discharge energy, E_d	[9,13,14,19,24,25,36–41]	MTTB, DPT, SI, TPP, PIV, PA
	Repetition rate, f_d	[23,34,41–46]	TPP, SI, PIV
	Discharge duration, T_d	[13,28]	TPP
Geometrical	Cavity volume, V_{ca}	[27,28,42,47–49]	SI, PIV, TPP
	Exit diameter, D	[21,22,47,50]	SI, TPP, PIV
	Throat length, L_{th}	[21]	TPP
	Electrode configuration	[21,26,49,51]	TPP, SI, PIV
	Orifice configuration	[50,52]	PIV, SI
Atmospheric	Ambient pressure, P_0	[38,43,45,53]	DPT, SI
	Ambient temperature, T_0	–	–
	Humidity, ρ_0	–	–

Schlieren imaging is so far the most widely used experimental technique to characterize the performance of PSJAs. The density gradient of the ensuing jet flow is integrated along the light ray direction and converted into different luminosity in the images. All the prominent flow structures including precursor shock waves, hot-jet plumes as well as vortex rings can be well visualized by this technique. Although Schlieren imaging is a qualitative technique, advanced post-processing methods have been proposed to extract quantitative information from the Schlieren images. Typically, the axial positions of pertinent flow structures at increasing time delays from discharge ignition are tracked, and the propagation velocities of the shock waves, the starting vortex ring and the jet front can be estimated [13,50]. It should be noted that the peak propagation velocity of the starting vortex ring or the jet font is only half of the peak jet exit velocity measured by PIV [33,52]. Additionally, by monitoring the time evolution of the spatially averaged grayscale within an interrogation window just above the exit orifice, the jet duration (T_{jet}) can be determined using a preset threshold value [21,25]. In [54], the relationship between light deflection angles and greyscale variations in the Schlieren setup is calibrated, and the phase-averaged density fields of plasma synthetic jets are derived under the assumption of axisymmetric flow.

PIV was employed by Cybyk et al. [9] and Ko et al. [55] to measure the developing flow fields of PSJs in quiescent condition, however no velocity vectors were resolved in the jet core region due to an absence of particles. They ascribed this limitation to the fast expansion of jet flow. In similar tests conducted by present authors (1 and 3), this issue only becomes significant at large energy deposition and can be solved by the intra-cavity seeding scheme proposed in [22]. With PIV measurements, the spatially averaged exit velocity ($U_e(t)$) can be directly evaluated as an integral of the radius-weighted jet velocity profile at the actuator exit ($x = 0$) [33]. Based on the

time-evolution of $U_e(t)$, the mean jet exit density (ρ_e) and its error band can also be estimated using the mass conservation law and a subsonic-throat-flow assumption [24]. The integral of the product of ρ_e and increasing exponents of $U_e(t)$ defines three crucial jet performance parameters, i.e., the expelled gas mass (M_e), impulse (I_p) and jet mechanical energy (E_m), as shown in Equation (3). T_{jet} is the jet duration determined from the zero-crossing moment of jet exit velocity.

$$\begin{cases} M_e = \int_0^{T_{jet}} \rho_e(t) U_e(t) A_e \cdot \mathrm{d}t \\ I_p = \int_0^{T_d} \rho_e(t) U_e(t) |U_e(t)| A_e \cdot \mathrm{d}t \\ E_m = \int_0^{T_d} 0.5 \rho_e(t) U_e^2(t) |U_e(t)| A_e \cdot \mathrm{d}t \end{cases} \tag{3}$$

As these parameters are closely related to the actuator geometry and input energy, three respective non-dimensional parameters can be derived as follows [33],

$$\begin{cases} M_e^* = M_e / (\rho_0 V_{ca}) \\ I_p^* = I_p / \sqrt{2 E_d \cdot \rho_0 V_{ca}} \\ \eta_m = E_m / E_d \end{cases} \tag{4}$$

where, ρ_0 and V_{ca} represent the ambient density and the cavity volume respectively. E_d is the discharge energy integrated from discharge voltage and current, namely $E_d = \int u_d i_d \, \mathrm{d}t$. I_p and η_m are interpreted as the "impulse" efficiency and the electro-mechanical efficiency pertaining to PSJAs.

Itt must be stressed here that for conventional synthetic jet actuators with sinusoidal exit velocity variation, various energy efficiency definitions are available, depending on whether the kinetic energy of suction flow should be taken into account and which jet reference velocity (e.g., time-mean ejection velocity, momentum-based ejection velocity) is used in the simplified expression of the jet kinetic energy [56,57]. As a comparison, the energy efficiency definition for PSJAs proposed in Equations (3) and (4) is more robust and less ambiguous. Firstly, the instantaneous kinetic energy flux is directly used for computing the total mechanical energy, which avoids the confusion created by the usage of different jet reference velocities. Secondly, for PSJs, the peak suction velocity is typically one order less than the peak jet velocity, and the kinetic energy incorporated in the suction flow is negligible (less than 10%) compared to the kinetic energy incorporated in the high-speed jet [33,46]. Consequently, whether suction flow is taken into account or not will incur rather minimal variation to the computed efficiency value for PSJAs.

3.1.2. Effect of Electrical Parameters on the Formation Process

During the formation process, electrical parameters serve as the input to the actuator system and mainly include discharge energy, repetition rate and discharge duration. Discharge energy is generally normalized by the internal energy of the cavity gas at rest, resulting in a non-dimensional energy deposition (ϵ), as shown in Equation (5) [20,25].

$$\epsilon = \frac{\int_0^{T_d} u_d(t) i_d(t) \cdot dt}{C_v \rho_0 V_{ca} T_0} \tag{5}$$

where, C_v and T_0 denote the constant-volume specific heat capacity and the ambient temperature, respectively.

The non-dimensional energy deposition (ϵ) plays a crucial role in tuning the intensity of the pulsed jets. Specifically, the energy deposition process is commonly described as a constant-volume heating process. The peak pressure ratio that can be reached inside the actuator cavity after the

arc heating is proportional to ϵ [37,58], and further determines the time-varying exit velocity in the jet stage. As demonstrated by the Schlieren and PIV data in Figure 5a, the peak jet velocity (U_p) increases monotonically, yet nonlinearly with the non-dimensional energy deposition [13,19,33,34,39]. This nonlinear relationship is demonstrated to be $U_p \propto \epsilon^{1/3}$ by Zong and Kotsonis in [33], under assumptions of constant electromechanical efficiency and self-similar exit velocity variation in the jet stage, which means doubling the peak exit velocity would require an eight times increase in the energy deposition. To validate this scaling law, the relative variations of peak jet velocity ($\Delta U_p = U_p/U_{p0}$) in each dataset are plotted against the relative increment of energy deposition ($\Delta\epsilon = \epsilon/\epsilon_0$) in Figure 5b, where U_{p0} is the peak jet velocity achieved at the lowest energy deposition level in each dataset (ϵ_0). As a result, different datasets collapse roughly on the same line in a logarithmic coordinate ($\Delta U_p = (\Delta\epsilon)^{1/3}$), and the residual errors can be ascribed to the biased assumption of constant electromechanical efficiency.

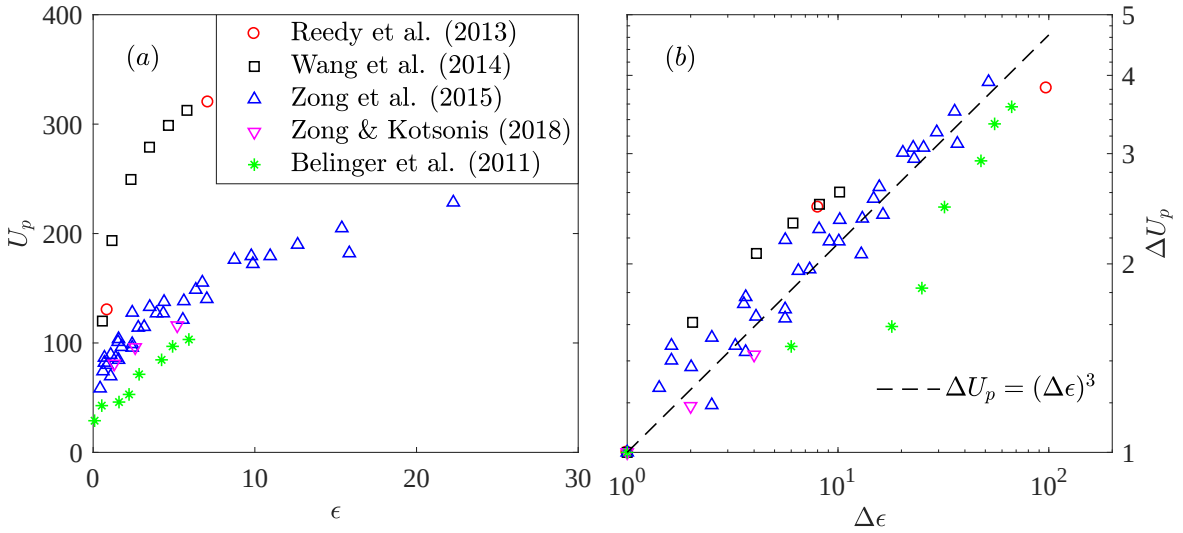

Figure 5. (**a**) Peak jet velocity at different non-dimensional energy deposition; (**b**) Relative variations of the peak jet velocity (ΔU_p) plotted against the relative increment of the non-dimensional energy deposition ($\Delta\epsilon$).

In addition, with increasing energy deposition, the jet duration time (T_{jet}) initially increases and then saturates [13,25]. The saturation at large energy deposition can be ascribed to the limited gas mass inside the actuator cavity. Keeping the above-mentioned trends of exit velocity and jet duration time in mind, it is straightforward to derive the conclusions that the expelled gas mass, jet impulse and jet mechanical energy will increase monotonically with the non-dimensional energy deposition, as has already been validated in [9,20,28,40].

The discharge repetition rate (f_d) affects the available refresh time and is typically normalized by the Helmholtz natural frequency of the actuator cavity (denoted as f_h) [23,31], resulting in a non-dimensional working frequency (f^*). Shown in Equation (6), f_h is a function of atmospheric parameters and actuator geometrical parameters. T_h and L_{th} denotes the Helmholtz natural period and the throat length, respectively.

$$\begin{cases} f_h = \dfrac{1}{2\pi}\sqrt{\dfrac{\gamma P_0}{\rho_0}}\sqrt{\dfrac{A_e}{V_{ca}L_{th}}} \\ f^* = \dfrac{f_d}{f_h} = \dfrac{T_h}{T_d} \end{cases} \tag{6}$$

The significance of the Helmholtz natural oscillation frequency can be interpreted by comparing the actuator to a spring-mass-damper system. Assuming the actuator cavity is initially at rest and

a small pressure disturbance is abruptly imposed to the actuator cavity (e.g., rapid compression by a piston). This disturbance leads to an uneven pressure across the actuator throat, which drives the fluid to escape from the actuator cavity (analogous to a "spring"). While the cavity gas is being ejected, the cavity pressure drops and the jet velocity decreases. Nevertheless, the ejection phase will not terminate at the moment of zero cavity pressure due to the inertia of the throat gas (analogous to "mass"). A negative cavity pressure is required to stop the ejection, which provides the driving force for the subsequent ingestion phase. The alternation between the ejection and ingestion phases will not cease until all the disturbance energy is damped out by viscous forces (analogous to a "damper").

Theoretically, at least one alternation between the ejection and ingestion phases is necessary to reset the actuator, thus the Helmholtz natural frequency can be interpreted as the theoretical limit working frequency of PSJAs [33], beyond which the intensity of pulsed jets deteriorates considerably. Evidences of this conclusion can be found in [34,42]. For the actuator used by Narayanaswamy et al. in [42], the Helmholtz natural frequency is estimated to be 10.7 kHz ($L_{th} \approx 2$ mm, exact value not provided). When this actuator is operated at a frequency (10 kHz) close to the Helmholtz natural frequency, considerable misfires were observed in one sequence as a result of the insufficient refresh time that breaks cycle–to–cycle repeatability [42]. In [34], the intensity of PSJs at increasing frequency was diagnosed by a total-pressure probe, and a "saturation frequency" was observed, above which the time-averaged jet total pressure (equivalent to thrust) no longer increases with the discharge frequency. The "saturation" frequencies of the two tested actuators (4 kHz for D = 1 mm, 6 kHz for D = 1.5 mm) agree well the Helmholtz natural frequency computed from Equation (6) (3.6 kHz and 5.4 kHz). Additionally, Zong et al. [34] concluded a linear relationship between the "saturation frequency" and the exit orifice diameter, which also agrees with Equation (6).

In the start-up process of the actuator, a transient stage consisting of several cycles is exhibited, where the mean cavity temperature increases cycle by cycle due to heat accumulation and the exit velocity variation in one period is not repeatable [16,23,34,46]. As illustrated by Figure 6 (reproduced from [46]), the transient stage is followed by a quasi-steady stage featuring approximately unchanged mean cavity temperature/density and excellent repeatability of the exit velocity variation from cycle to cycle. Note that these two criteria (i.e., invariant mean cavity temperature and repeatable exit velocity) may not be reached at the same moment. For example, the exit velocity variation in Figure 6a takes only 20 cycles to reach the steady stage, whereas the mean cavity temperature/density in Figure 6 does not stabilize until 130 cycles have elapsed. This findings will be retrieved also in the numerical and the analytical simulations shown in the next sections. By definition, in the steady stage two relations shall be satisfied, namely the mass conservation inside the actuator cavity and the energy equilibrium during one actuation cycle. Starting from these two relations, Zong and Kotsonis [46] derived that the mean cavity temperature/density in the steady working stage increases/decreases monotonically with the repetition rate, as shown in Equation (7) .

$$\begin{cases} \dfrac{\rho_{ca}}{\rho_0} = \dfrac{T_0}{T_{ca}} = \dfrac{2}{1+\sqrt{1+4(2-\sqrt{2})f_d/f_c}} \\ f_c = \dfrac{(2-\sqrt{2})h_c\gamma S_{in}T_0}{E_h} \end{cases} \tag{7}$$

where, f_c is termed as the thermal cut-off frequency, below which the influence of repetition rate on cavity density is marginal ($\rho_{ca}/\rho_0 > 0.707$); h_c and S_{in} are the convective heat transfer coefficient and the area of the cavity internal surface, respectively; γ and E_h denote the specific heat capacity ratio and the arc heating energy, respectively. Note that E_h is lower than the discharge energy E_d used in Equation (5) due to inevitable gas heating losses including ionization, radiation and sheath losses [28,42,59].

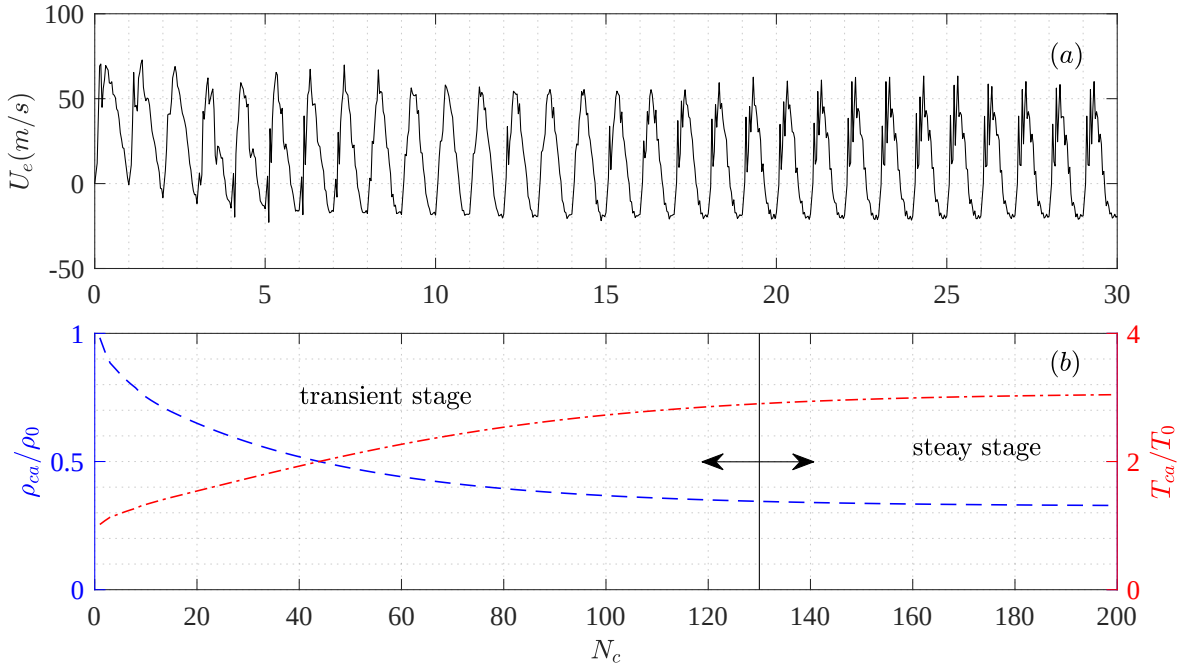

Figure 6. (**a**) Time-resolved jet exit velocity in the first 30 cycles after discharge ignition ($f^* = 1.05$); (**b**) Evolution of the mean cavity temperature (dash line) and mean cavity density (dash-dot line) in the initial 200 cycles after start-up. N_c is the cycle number (t/T_d).

The validity of Equation (7) can be justified from the experimental results in [11,13,34]. Belinger et al. [13] measured the mean temperature of the actuator cap (material: brass) at a fixed discharge frequency of 100 Hz, using an infrared camera. As a result, the cap temperature increases monotonically with the discharge energy, which is consistent with Equation (7). The peak cap temperature at a discharge power of 10 W reaches approximately 400 K and 600 K for capacitive and inductive discharge, respectively. The high cap temperature in case of inductive discharge is ascribed to the earlier ejection of cavity gas. Specifically, as the energy deposition rate for inductive discharge is much lower than that of the capacitive discharge, the majority of the gas heating energy is unable to be transported out of the actuator cavity by mass exchange, due to the earlier termination of gas ejection with respect to energy deposition. Consequently, the residual heating energy has to be dissipated to the external actuator shell via heat transfer, resulting in the reported high temperatures for the cap. Caruana et al. [11] compared the temperature of two caps made from different materials (aluminium vs. brass). Under the same operating condition (frequency and energy), the aluminium cap exhibits a lower cap temperature and a higher jet total pressure than the brass cap, largely attributed to the higher thermal conductivity of aluminium in comparison to brass. This agrees well with the effect of the heat transfer coefficient as indicated by Equation (7). In Zong et al.'s study [34], a K-type thermocouple was inserted into the actuator to measure the temperature of the cavity wall at increasing discharge frequency. A similar increasing trend was demonstrated, and the peak cavity wall temperature reaches approximately 900 K at $f_d = 6$ kHz. As the exit orifice diameter increases, the peak cavity wall temperature drops.

As a comparison to the widely recognized conclusions made on the mean cavity density/temperature, the effect of repetition rate on the jet exit velocity remains disputable. In [13], Belinger et al. measured the peak jet total pressure with a modified pressure transducer (equivalent to the peak jet Mach number, according to Equation (1)), and a decreasing trend of the jet Mach number at increasing frequency was observed for both capacitive and inductive discharge. This decreasing jet total pressure can be attributed to either the decreasing jet density, or the decreasing exit velocity

or both. In [44], a pulsed DC power supply was adopted to feed the actuator, and the peak jet velocity determined from high-speed Schlieren imaging (89 m/s–97 m/s) changes marginally with the actuation frequency in the range of 100 Hz–1000 Hz. This trend was also confirmed by the PIV results shown in [46]. Sary et al. [16] performed a numerical simulation based on the actuator used by Belinger et al. in [13]. As a result, the peak exit velocity changes marginally at $f_d < 1$ kHz and drops significantly afterwards. These observations are roughly consistent, however contradicting the results predicated by the analytical model in [34], where the peak jet velocity increases monotonically with the repetition rate.

The following discussion aims at reconciling these seemingly contradicting observations. Under the assumptions that the energy deposition stage is a constant-volume heating process and the jet stage is an isentropic expansion process, respectively, the peak exit velocity (U_p) in the steady stage can be estimated by Equation (8), where η_h is the heating efficiency. $P_{t,p}$ is the peak cavity pressure after energy deposition; M_p and T_p denote the peak jet Mach number and the corresponding jet temperature, respectively.

$$\begin{cases} \dfrac{P_{t,p}}{P_s} = 1 + \eta_h \epsilon = (1 + \dfrac{\gamma - 1}{2} M_p^2)^{\frac{\gamma}{\gamma - 1}} \\ U_p = \sqrt{\gamma R T_p} \cdot M_p \end{cases} \tag{8}$$

In [34], constant discharge energy and heating efficiency are prescribed as the inputs of the analytical model. Based on Equation (8), M_p is expected to remain unchanged while U_p will increase monotonically with the repetition rate as a result of the increasing temperature. For capacitive arc discharge with constant discharge energy [44,46], the heating efficiency drops at high frequency due to the reduced cavity density [60], leading to a slightly decreasing peak jet Mach number. The decreasing trend of M_p and the increasing trend of T_p at high repetition rate are somehow mutually balancing, leading to an approximately unchanged peak jet velocity as observed by Zong and Kotsonis [46] and Jin et al. [44]. In [21], the energy-storage capacitor was charged by a DC power supply, and the discharge energy drops at high repetition rate due to the insufficient charging time. As a result, it is rather expected to observe a trend of decreasing peak jet velocity when f_d increases.

Based on the above analysis, it can be concluded that the discharge circuits have a significant effect on the behaviour of peak exit velocity at increasing frequency. Despite the fact that U_p may increase for cases of constant heating efficiency, the three integral parameters defined in Equation (3) unexceptionally exhibit a decreasing trend with increasing frequency [13,34,46], indicating a dominant role of the reduced jet density. To compensate the negative effects brought by the low cavity density at high-frequency operation, Emerick et al. [50] connected an external air supply to the actuator cavity to assist the refilling. This approach can indeed improve the jet intensity, nevertheless complexities the actuator structure, and diminishes some of the weight advantages of these actuators.

The effect of discharge duration on the intensity of pulsed jets are experimentally examined in [13,28]. Compared to the case of capacitive discharge where the energy is deposited in less than 10 μs, PSJs generated by inductive discharge (discharge duration: O (100 μs)) exhibit a lower peak jet velocity but a longer jet duration time [13]. For pulsed DC discharge with fixed energy deposition, both the heating efficiency and the thermodynamic cycle efficiency decrease with increasing discharge duration [28].

3.1.3. Effect of Geometrical and Atmospheric Parameters on Formation Process

Geometrical parameters mainly comprise cavity volume, exit diameter, throat length, electrode configuration and so on. Effects of the first three of these parameters have actually been taken into account by the two dimensionless parameters defined in Equations (5) and (6). When the cavity volume increases, the peak jet velocity drops as a result of the decreasing non-dimensional energy deposition, nevertheless the jet duration time increases due to an increasing Helmholtz natural

oscillation period [47,48]. The overall efficiency of PSJAs (η_m) decreases with increasing cavity volume, not only because the temperature ratio that can be reached after the energy deposition stage is lowered, but also because the arc heating inside the actuator cavity becomes more localized which decreases the heating efficiency [28,49].

With increasing orifice diameter, the jet duration time decreases as a direct consequence of higher mass flow rate, whereas the peak jet velocity and the three integral parameters defined in Equation (3) remain approximately unchanged [21,24,47]. Additionally, based on Equation (6), the theoretical limit working frequency of PSJAs increases linearly with orifice diameter. Variation of the throat length doesn't affect the peak jet velocity and the jet duration time of PSJAs in single-shot mode. Nevertheless, a longer throat length leads to a lower Helmholtz frequency and a fast deterioration of the jet intensity at high-frequency operation [21]. With increasing electrode distance and unchanged energy deposition, the arc heating region is enlarged and the overall efficiency of PSJAs is improved, leading to a higher peak jet velocity as well as a longer jet duration [21]. The ratio of the arc heating volume to the cavity volume is defined as the dimensionless heating volume, which quantifies the uniformity of arc heating. The electro-mechanical efficiency of PSJAs is demonstrated to increase significantly with the dimensionless heating volume [49]. This conclusion can somehow be validated from the results from [42] a posteriori. In their study, the dimensionless heating volume was kept unchanged. Two cases with different cavity volume (20 mm^3 and 40 mm^3) were tested with Schlieren imaging, and similar jet trajectories were obtained consequently.

Atmospheric parameters (e.g., pressure, temperature and humidity) define the environment in which the actuators are operating. Driven by the need of implementing flow control technology to air vehicles cruising at high-altitude, effects of the ambient pressure on the performance of PSJAs were investigated extensively. In [37,43,53], the discharge energy is fixed, and the dimensionless energy deposition defined by Equation (5) increases with decreasing ambient pressure/density. As expected, an increasing trend of the peak jet velocity as well as the peak nozzle pressure ratio (equivalent to peak jet Mach number) is exhibited while the ambient pressure drops. In contrast, in [45], the discharge energy depends on the breakdown voltage of the inter-electrode gap and decreases monotonically with the decreasing ambient pressure. Consequently, the peak jet velocity changes marginally with the ambient pressure.

3.1.4. Evolution Process

A representative evolution sequence of the plasma synthetic jets in quiescent flow and the corresponding exit velocity variation in one cycle is shown in Figure 7 (reproduced from the PIV dataset recorded by Zong and Kotsonis in [33]). Several prominent flow structures have been observed in the evolution process [19,22,61], including compression/expansion waves (smoothed out in Figure 7a due to phase-averaging operation), a train of vortex rings (Figure 7c), high-speed jet (Figure 7b–d) and localized weak suction (Figure 7e). Similar to the scenario of shock tube problems, compression and expansion waves are initialized from the interface between the arc-induced high-pressure zone and the unaffected low-pressure zone [21,42]. During the subsequent propagation, part of these waves are directly released from the exit orifice, while the rest are reflected back by the inner cavity wall and lag behind. Consequently, multiple compression/expansion waves are issued out of the cavity, regardless of the amount of peaks in the discharge waveforms [19,39]. For round orifices, the velocity difference across the propagating compression waves decreases linearly with the radial propagation distance in logarithmic scaling, and the intensity of these waves increases with increasing exit orifice diameter [22]. Additionally, a slight density rise is exhibited behind the compression waves. This density rise peaks at approximately $0.1\rho_0$ and decays to a negligible value after 200 μs [54].

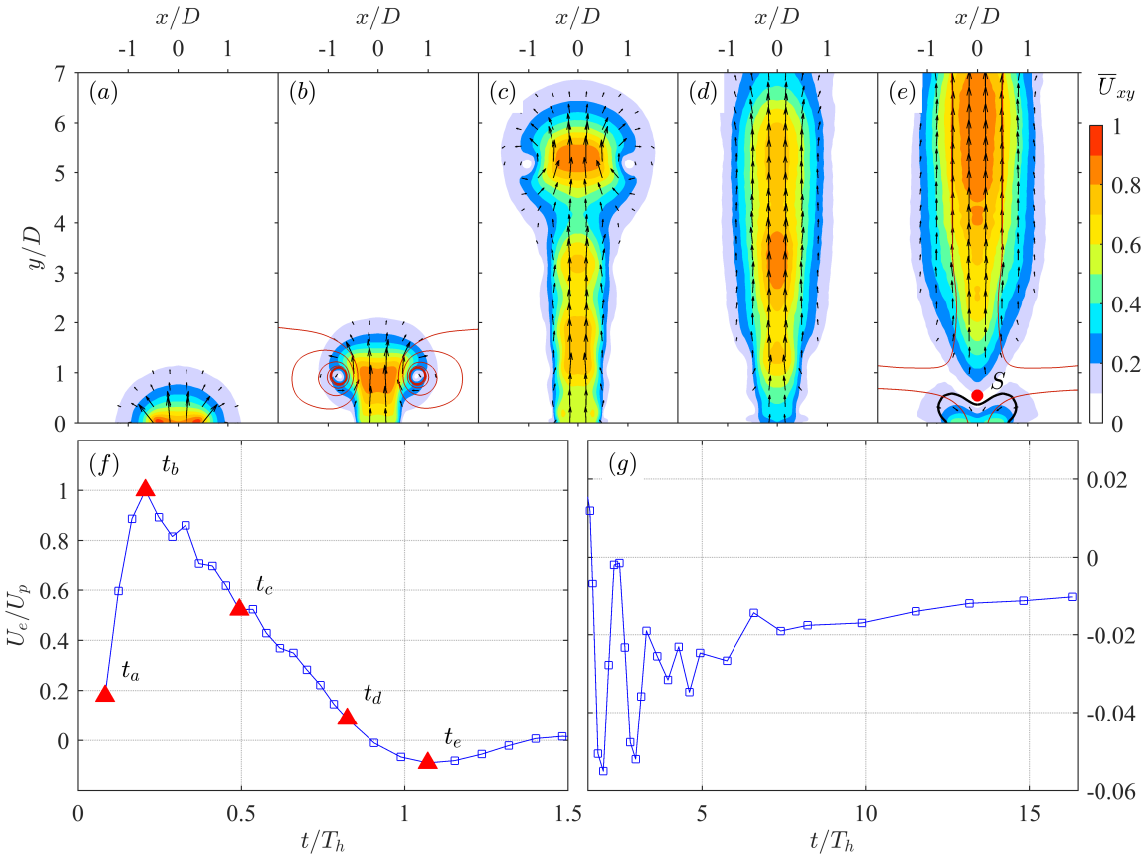

Figure 7. (**a**–**e**) Phase-averaged evolution of PSJs at $\epsilon = 2.6$ and $f^* = 0.06$ (reproduced from the dataset measured by Zong and Kotsonis in [33]). From left to right, the phases displayed are $t_a = 50$ µs, $t_b = 125$ µs, $t_c = 300$ µs, $t_d = 500$ µs, and $t_d = 650$ µs. The in-plane velocity (U_{xy}) is normalized to an identical range of 0–1 by dividing their respective maxima (20 m/s, 120 m/s, 91 m/s, 38 m/s, 23 m/s). The magnitude and direction of the normalized in-plane velocity ($\overline{U}_{xy}$) are displayed as contours and vectors, respectively. The thin red lines superimposed on (**b**,**e**) are streamlines. The thick black line in (**e**) represents the velocity contour line of $U_x/U_p = -0.01$. (**f**,**g**) Time evolution of the spatially averaged exit velocity (U_e) in one cycle. The peak exit velocity ($U_p = 116$ m/s) is used for normalization. Note that different scales are used for the phases before and after $t/T_h = 1.5$. The five phases corresponding to Figure 7a–e are indicated in the exit velocity curve by red triangles.

Vortex rings are shed from the exit orifice as a result of the impulsive starting jets. In the case of conventional starting jets, depending on the stroke ratio defined by Equation (9), either isolated vortex rings ($L^* < 4$) or vortex rings ensued by a trailing jet column ($L^* > 4$) will be formed [62]. L_s is the stroke length.

$$L^* = \frac{L_s}{D} = \frac{1}{D}\int_0^{T_{jet}} U_e(t)\mathrm{d}t \tag{9}$$

For PSJs, the stroke ratio is proportional to the non-dimensional energy deposition. At increasing non-dimensional energy deposition, three different evolution regimes are observed using Schlieren imaging [25], including weak shock waves without noticeable vortex rings or jets (small ϵ), weak trailing jets with detached vortex rings (intermediate ϵ), and strong bright jets that are always connected with the starting vortex rings (large ϵ). The last two regimes described here are consistent with that of the conventional starting jets to some extent. Apart from the starting vortex ring which always resides in the jet front (Figure 7b), secondary vortex rings located in the jet shear layer are perceived in [19,22]. These shear layer vortices are promoted by the small oscillations in the exit

velocity which can be caused either by the shock wave reflections inside the actuator or by the inherent oscillation of the discharge waveforms (capacitive discharge) [46,63].

Within one cycle, the propagation velocity of the front vortex ring exhibits an initial rapid increase followed by a gradual decrease [22,33]. For round orifice, the peak propagation velocity reached at $x = 2D$ is approximately half of the peak jet exit velocity ($0.43U_p$), regardless of the energy deposition and the repetition rate. The vortex ring circulation shares a similar variation trend as the propagation velocity, and the peak circulation value is approximately $0.62U_pD$. In the case of slot orifice, an elongated vortex ring is ejected and undergoes axis-switching during the subsequent evolution [52]. The axis-switching phenomenon is attributed to the complex self-induction and mutual interaction between different parts of the ring [64]. Compared to the round orifice with equal exit area, PSJs issued from the slot orifice exhibit a much higher entrainment rate but relatively lower jet penetration [52].

In the later phases of the jet stage, a weak suction flow is initiated from the peripheries of the jet exit orifice and grows steadily inwards [46]. As a result of the concurrent weak suction and the ongoing jet expulsion, a saddle point is observed at the near-exit region ("S" in Figure 7e) [22,33]. The suction affected length derived from the axial position of the saddle point increases slightly with time during one cycle (peak value: $1D$). Additionally, the suction velocity in the refresh stage is not steady. Periodical fluctuations due to the Helmholtz natural oscillation are exhibited, as evidenced by Figure 7g. The peak suction velocity (typically less than 10 m/s, $-0.1U_p$ in Figure 7g) increases with both the energy deposition and the repetition rate [33].

The time-averaged velocity fields of plasma synthetic jets bear significant similarity with that of steady jets, in the sense that an approximately linear expansion of the jet width (w_h) is exhibited [33,46]. With increasing repetition rate, the jet spreading rates of PSJs range from 0.17 to 0.09, which lie in between the steady jets (0.09–0.11) and the piezoelectric synthetic jets (0.13–0.195) [46]. The jet centreline velocity ($\overline{U}_{cm}$) shows an non-monotonic variation along the axial direction, and the normalized peak jet centreline velocity ($\overline{U}_{cm}/f_dL_s$) decreases from 1.5 to 1.0 with increasing frequency. When the jet velocity profiles at different axial locations are normalized by the centreline velocity and the jet width, a good collapse is obtained [33]. The entrainment coefficients of PSJs change between 0.19 and 0.26, which are twice as high as the values for steady jets.

3.2. Numerical Studies

An accurate simulation of a complete PSJ operating cycle needs to incorporate multi-scale phenomena, such as Joule heating, heat radiation, Lorentz forces, arc-electrode or arc-wall interactions and real-gas effects. Generally speaking, one way to take into account all these phenomena consists of solving the Navier–Stokes or Euler equations with the addition of electro-magnetic source terms [65].

Initial attempts to simulate the behaviour of a PSJ device were made in [47,58], considering only one discharge pulse. Unsteady compressible simulations were carried out with CFD^{++} commercial solver, with the energy deposition stage modelled as an instantaneous constant-density heating process and the heat deposited in the bottom 40% of the chamber volume. Results showed that the issued PSJs were promising for high-speed flow control.

Few years later, a much detailed simulation, also focused on the energy deposition process within the actuator cavity in single-shot mode, was presented by Dufour et al. in [15]. The model, based on previous studies in [13,14], assumed a two-dimensional axisymmetric flow with all variables dependent only on the radial and axial coordinates. Euler equations, consisting of the conservation of mass, radial and axial momentum and energy, were solved. Real-gas effects were considered, and the arc was assumed in local thermal equilibrium (LTE). The Joule heating effect was modelled as an energy source term in the energy equation. The electric field necessary for computing the Joule heating was determined from an equivalent RLC circuit of the external discharge circuit. Specifically, the circuit was composed of a capacitor, an inductor and a fixed resistor corresponding to the parasitic parameters of the connecting wires, two serially connected variable resistors representing the voltage drop on arc plasma and the energy loss in plasma sheath, respectively.

The unknowns in the RLC circuit are the current and the capacitor voltage. As the model is unable to capture the gas breakdown process, non-uniform initial conditions with a thin high-temperature zone between the electrode gap corresponding to the just ignited discharge channel should be specified to launch the simulation. Results obtained at a total deposited energy of 7.7 mJ show that the cavity pressure rapidly increases in a few µs, generating a blast wave, which is quickly evacuated outside, meanwhile the temperature within the arc core reaches an order of O (10^4) K. Moreover, during the energy deposition, the propagating shock wave induces a hot area expanding outwards from the electrode gap. Two toroidal eddies are subsequently created, constraining the development of the hot area. After the energy deposition is finished, the toroidal eddies evolves into a bubble shape and gradually escape from the electrode gap.

Taking advantage of the previous work, numerical investigations of the jet evolution outside the cavity in both single-shot mode and repetitive regime were carried out by Sary et al. in [16]. An explicit shock-capturing scheme (Roe scheme) was used for solving the fluid equation system, to sufficiently capture the high-velocity jet propagating into a low-velocity medium. Simulations of the single-shot mode show that the energy deposition produces an overpressure within the cavity, which forces the air to exit form the orifice. The jet front, in an arrow shape, reaches a velocity on the order O (100) m/s. Furthermore, a vortex ring is formed near the jet front, propagating along the jet axis, as shown in Figure 8. The spatial distribution of jet temperature in the ejection stage (not shown) exhibits a similar arrow shape as the exit velocity, since the high-velocity gas originates from the high-temperature high-pressure arc discharge zone. The instantaneous peak jet temperature can reach 3000–4000 K based on the numerical simulation results in [16], which is much higher than the value measured by Ko et al. [55] (1600 K), probably due to the different energy deposition level. During the refresh stage, the high-temperature jet core region has propagated sufficiently away from the exit orifice, and the near-exit region is dominated by the ingestion of ambient gas, thus leading to a relatively uniform distribution of low gas temperature (i.e., close to ambient temperature) outside the actuator cavity.

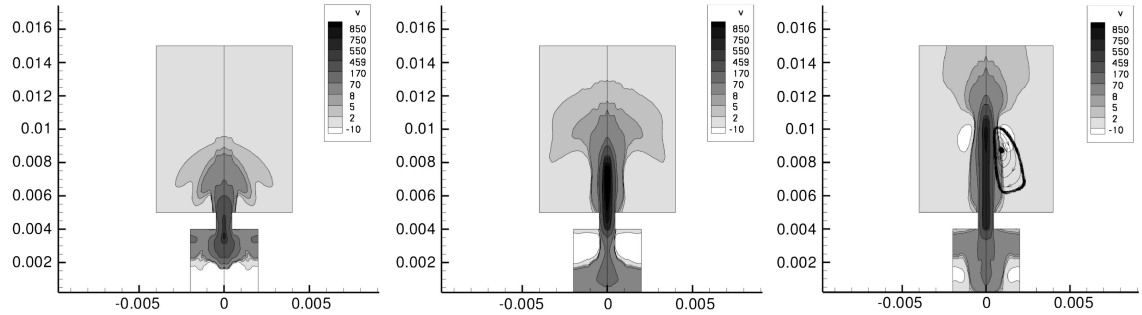

Figure 8. Velocity distribution in the jet at (**left**) 12, (**middle**) 25, (**right**) 37 µs after the breakdown [16].

Sary et al. also simulated the transient working behaviour of the actuator in the first 25 cycles after discharge ignition, with a discharge energy of 7 mJ and a repetition rate of 1 kHz. Figure 9 reports the evolution of the main thermodynamic quantities. It is interesting to observe that, for these conditions, the periodic behaviour seems to be obtained after 10 pulses. However, as stated in the Section 3.1.2, the mass and mean temperature within the cavity require more time to reach the dynamic equilibrium. Furthermore, the ejected mass in each cycle is approximately 10% of the initial cavity mass. The mean cavity temperature increases monotonically and exceeds 900 K in the steady stage. The peak overpressure during each cycle remains around 0.4 bar, with a total enthalpy variation of 6.7 mJ for each pulse.

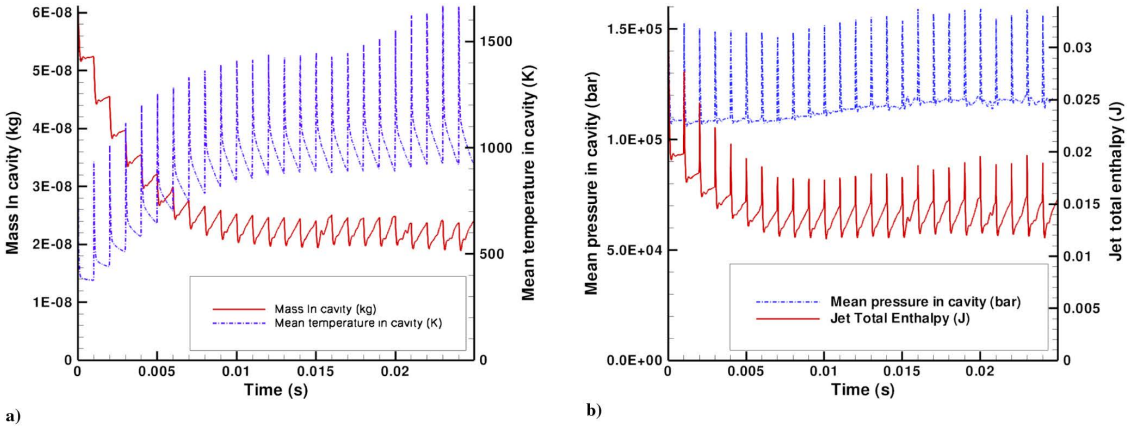

Figure 9. Temporal evolution of: (**a**) mass and mean temperature versus time; (**b**) mean pressure and total jet enthalpy versus time [16].

Laurendeau et al. [63] used an LES approach to capture the transient development of a PSJ, using the previous energy deposition model as a source term [15]. These simulations dealt with the ejection phase only, representing the cases where an actuator is working at a sufficiently low frequency such that no interaction between adjacent jets can be expected. Two different energy source terms (a time-invariant one and an unsteady one) were analysed, and the trajectory of the jet front extracted from the simulations were validated with Schlieren data. Figure 10 reports the vortex structures at the exit of the nozzle visualized by the contour of vertical density gradient. Note that the break of secondary vortex structures can be attributed to azimuthal instability, and the presence of a pressure wave is consistent with the experimental findings of Zong et al. [25] in Section 3.1.4.

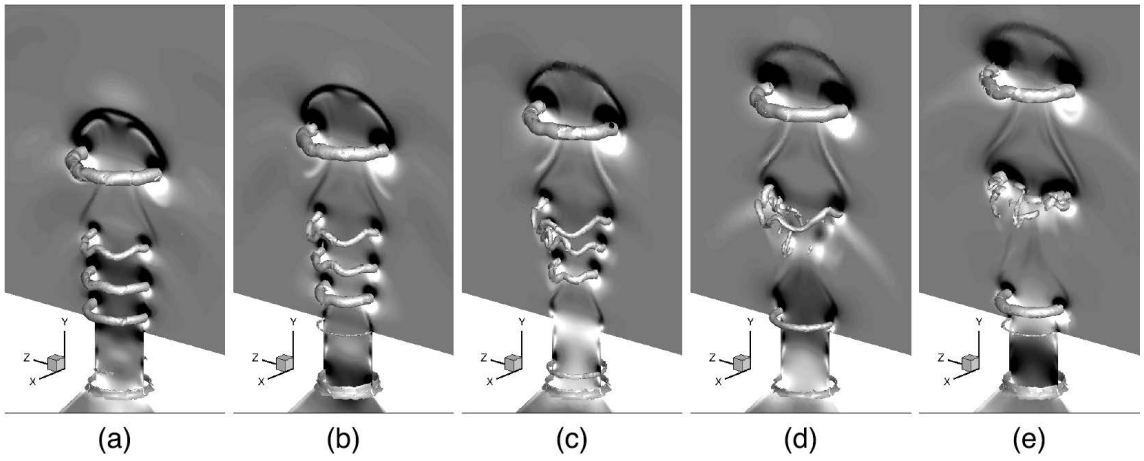

Figure 10. Vertical density gradient (vertical plan) and Q iso-criteria surfaces (3D) for (**a**) $t = 60\,\mu s$; (**b**) $t = 65\,\mu s$; (**c**) $t = 70\,\mu s$; (**d**) $t = 75\,\mu s$; (**e**) $t = 80\,\mu s$ [63].

In [66], Laurendeau et al. also proposed a numerical model to study the PIV measurement uncertainty in jet characterization. The model represents an improvement of the previous versions, coupling the energy source term directly within the LES computations.

3.3. Theoretical Models

Theoretical models prove to be useful tools for the conceptual design of the actuator system, as the temporal response of the actuator to repetitive energy deposition can be predicted in short time and with minimal computation resources. However, these models are purely thermodynamic, with the gas discharge phase and the plasma heating process unaccounted. To faithfully reproduce the actuator performance with these models, the net gas heating energy, regarded as one of the most

crucial model input parameters, has to be specified in high accuracy. Typically, the electrical energy provided by the discharge circuitry is predefined, thus the net gas heating energy can be derived by a proper estimation of the discharge and gas heating efficiency. These unknown efficiency values, which can bring noticeable uncertainties to the predicted actuator performance, are dependent on the discharge waveforms, electrode configuration and atmospheric condition, as will be discussed thoroughly in Section 4.

So far, several reduced-order models with increasing complexity have been proposed. The first model was presented by Haack et al. in [37], where the governing equations of the three working stages were derived as one-dimensional PDEs (Partial Differential Equations). The energy deposition stage was approximated as an instantaneous heating process, while the jet stage was considered to be isentropic. As a result, the model is capable of capturing the choked or unchoked flow conditions at the nozzle exit, but unable to retrieve the refresh stage, thus limited its application in the single-shot working mode of the actuator. Another attempt was made by Anderson Knight in [20], who carried out an analytical analysis of the force and impulse generated by single jet pulse. The model was validated with two-dimensional numerical simulations, and an explicit relation between the dimensionless energy deposition and the dimensionless impulse was derived. They proved that an array of PSJ devices produces sufficient force to replace an aerodynamic surface for flight control.

Recently, Zong et al. [34] proposed a lumped-element model, able to predict both the whole cycle characteristics and the repetitive working conditions of the actuator. A three-dimensional numerical simulation was carried out to define a linear model describing the heat transfer mechanisms between the actuator cavity and external environment. Two cases with the jet stage assumed to be either isentropic or politropic, were considered. The model was validated with the experimental data of the time-averaged jet total pressure and the cavity wall temperature. Later on in [28], the model was further improved by incorporating the discharge/heating efficiency, and the real gas effects.

Following the research line of the lumped models, a new model was presented in [23]. It is able to predict the time variation of all thermodynamic variables in the cavity as well as the jet velocity at the exit orifice, as functions of the operating frequency. The governing equations are fully based on aerodynamics and are enforced on the whole control volume without the isentropic assumption. The correct simulation of the refresh stage is guaranteed by the inertial term included in the unsteady Bernoulli's equation. Furthermore, the model was validated first through a comparison with data available in literature, and then with measurements performed on a house-made PSJA [31]. As this model can be considered as an extension of the others, more details are provided as follows. The actuator is modelled as a cylindrical cavity with an internal volume of V_{ca}, and a nozzle of length L_{th} and diameter D. The governing equations are based on two main assumptions. First, the model is lumped, namely the thermodynamic and transport properties are averaged in the whole cavity volume. Furthermore, to consider the real gas effects at high cavity temperature, the cavity gas is considered at local thermodynamic equilibrium [67].

3.3.1. Energy Deposition

Energy deposition refers to the process in which electrical energy is converted into the internal energy of cavity gas by virtue of arc heating. This process is non-ideal, exhibiting inevitable energy losses due to various electrical and physical effects [27,28]. Within the present model, an efficiency factor (η_k), considering the losses related to the parasitic resistance of connecting wires as well as the non-uniform heating effect of arc discharge, has been introduced, with typical values between 20% and 50%. As will be detailed later on in Section 4, this efficiency factor is essentially the product of discharge efficiency and equivalent uniform heating efficiency, $\eta_k = \eta_d \cdot \eta_h$.

When the discharge duration (T_{dis}) is much lower than the time-scale of jet expulsion (T_h), the energy deposition process can be considered instantaneous as negligible amount of the gas will escape from the actuator cavity. Usually this is the case for capacitive discharge. Considering a typical scenario where the wire inductance and the capacitance are on the order of 1 μH and 1 μF

respectively, the discharge time-scale for capacitive discharge would be $O(1\ \mu s)$, two orders lower than the typical jet expulsion time ($O(100\ \mu s)$). As such, it is safe to model the energy deposition stage as a constant-volume heating process. The state variables in the cavity before and after this process (distinguished by the superscript, i and $i+1$) are linked with the following equation set,

$$\begin{cases} \rho_{ca}^{i+1} = \rho_{ca}^{i} \\ T_{ca}^{i+1} = T_{ca}^{i} + \dfrac{E_h}{C_v V_{ca}\, \rho_{ca}^{i} T_{ca}^{i}} \\ p_{ca}^{i+1} = \rho_{ca}^{i} \cdot R(T_{ca}^{i+1}) \cdot T_{ca}^{i+1} \end{cases} \tag{10}$$

where ρ, T and p are the density, temperature and pressure, respectively. Subscripts associated to these symbols indicate the location where these parameters are evaluated, e.g., *ca*–actuator cavity, *e*–nozzle exit. $R(T_{ca})$ is the gas constant as a function of cavity temperature to include compressibility effect, i.e., $R(T_{ca}) = R_0\, f(T_{ca})$, with R_0 being the air gas constant in standard condition. E_{total} is total energy provided by the power supply system. $E_h = \eta_k \cdot E_{total}$ is the net energy available for gas heating.

3.3.2. Jet and Refresh Stages

During the jet stage, high-pressure fluid exhausts through the orifice, converting its increased internal energy into the kinetic energy. This phase can be simulated as the discharge process of a reservoir connected to the external ambient by means of a relatively short nozzle or orifice. The application of the mass conservation law to the system composed of the reservoir and the nozzle leads to the following relationship:

$$\frac{d\rho_{ca}}{dt} = -\frac{\rho_e\, U_e\, A_e}{V_{ca}} \tag{11}$$

with U_e indicating the exit velocity, A_e the exit orifice area, t the time.

The energy equation inside the whole cavity volume is enforced as follows:

$$\left[\rho_{ca}\frac{d}{dt}(u_c) + u_c\frac{d}{dt}(\rho_{ca})\right] V_{ca} + \rho_e \left(h_e + \frac{U_e^2}{2}\right) U_e A_e + \dot{Q} = 0 \tag{12}$$

where u and h are the internal energy and thermodynamic enthalpy, respectively, and $\dot{Q}$ is the total amount of heat power exchanged through the entire surface of the system.

It is worth noting that Equation (12) is only valid for a discharge time-scale of $T_{dis} \sim O(1\ \mu s)$. For cases with long discharge time, the energy deposition can no longer be considered as a constant-volume process, because the ejection and the heating processes occur simultaneously. In this specific scenario, the energy deposition stage does not need to be modelled independently. Rather, it can be treated as a special jet stage with both heat input (arc energy discharge) and output (heat losses through the actuator walls) terms [28]. By combining Equations (10) and (12), the following relation is obtained:

$$\left[\rho_{ca}\frac{d}{dt}(u_c) + u_c\frac{d}{dt}(\rho_{ca})\right] V_{ca} + \rho_e \left(h_e + \frac{U_e^2}{2}\right) U_e A_e + \dot{Q} - \frac{E_h}{T_{dis}} = 0 \tag{13}$$

The application of the compressible unsteady Bernoulli's equation, between a point inside the cavity (where the flow velocity is practically null) and the exit section of the nozzle, yields a third equation for these phases:

$$u_c + \frac{p_c}{\rho_c} = u_e + \frac{p_e}{\rho_e} + L_{Th,e}\frac{\partial U_e}{\partial t} + K\frac{|U_e|\, U_e}{2} \tag{14}$$

where K is the head loss coefficient, including entrance/exit losses at exit orifice; $L_{Th,e}$ is the modified effective length, representing the distance between the two points of application of Bernoulli's equation. The choice of the values for the head loss coefficient and the effective length has been treated in various previous papers. For piezo-driven synthetic jets, usually these terms have been determined by making a best fitting between numerical and experimental data or by using some empirical expressions [68]. Due to the lack of literature works on this topic for PSJAs, the previous quantities have been considered as fitting parameters and their values have been determined by matching the results of the lumped model with numerical simulations made with the OpenFOAM code. The effective orifice length has been evaluated as: $L_{Th,e}/D = L_{Th}/D + \Delta L_{Th,e}$, setting $\Delta L_{Th,e} = 1.5$ and $K = 1.78$, making a best fit with the CFD numerical results. Note that for these simulations, the energy deposition has been assumed instantaneous.

Another convenient equation for the flow along the nozzle is the classic isentropic relationship linking the thermodynamic properties inside the cavity to those at the orifice exit:

$$T_{ca} = T_e \frac{c_p(T_e)}{c_p(T_c)} \left[1 + \frac{\gamma(T_e) - 1}{2} M_e^2\right] \tag{15}$$

where M_e is the exit Mach number, and γ is the specific heats ratio expressed as a function of the temperature.

The exit flow condition, namely choked or unchoked flow, determines the equation required to close the problem. The establishment of either of these two conditions depends on the critical ratio of the cavity pressure to the exit pressure, i.e.,

$$\left.\frac{p_{ca}}{p_e}\right|_{cr} = \left(\frac{\overline{\gamma} + 1}{2}\right)^{\frac{\overline{\gamma}}{\overline{\gamma}-1}} \tag{16}$$

where $\overline{\gamma}$ is the mean value between the two states (i.e., cavity and exit section) involved. If the pressure ratio, after the energy deposition, is greater than or equal to that computed with Equation (16), the flow is choked, otherwise an unchoked regime is assumed. For choked flow, the nozzle exit condition is that the exit Mach number is sonic; otherwise the Kutta condition is retrieved. All the governing equations, written for both the choked and the unchoked case, can be found in [23].

The previous calibration process allows one to determine the actuator response (thermodynamic quantities within the cavity as well as the jet velocity exit) once the actuator geometrical parameters and the discharge waveforms (power and discharge time) have been defined. Nevertheless, to match the model results with the experimental ones, the unknown efficiency factor has to be tuned with a best-fit procedure [31].

3.3.3. LEM Results

Figure 11 depicts the time variation of the major thermo-fluid-dynamic quantities, such as jet exit velocity (U_e), mean cavity pressure (P_{ca}), temperature (T_{ca}) and cavity mass ($\overline{M}_{ca}$), monitored during the first cycle after start-up. In this case an instantaneous energy deposition is considered. Figure 11 (left) shows that the initial energy discharge produces a sudden increase of pressure (from the ambient value), which forces the air to exit from the orifice in a few microseconds. The jet velocity, in fact, reaches its maximum at about 30 µs after the discharge, then decreases rapidly and fluctuates slightly around zero. During one cycle the actuator ejects about 10% of its initial cavity mass. The mean cavity temperature, after the steep rise caused by the electrical discharge, first decreases sharply due to the convective enthalpy exchange induced by the issuing fluid flow, then slowly because of heat transfer effects, as shown in Figure 11 (right). Note that all quantities have been reported in their non-dimensional form; in particular the reference variables are: peak jet exit velocity (U_p), ambient pressure (P_0), ambient temperature (T_0) and initial cavity mass ($\overline{M}_{c0}$).

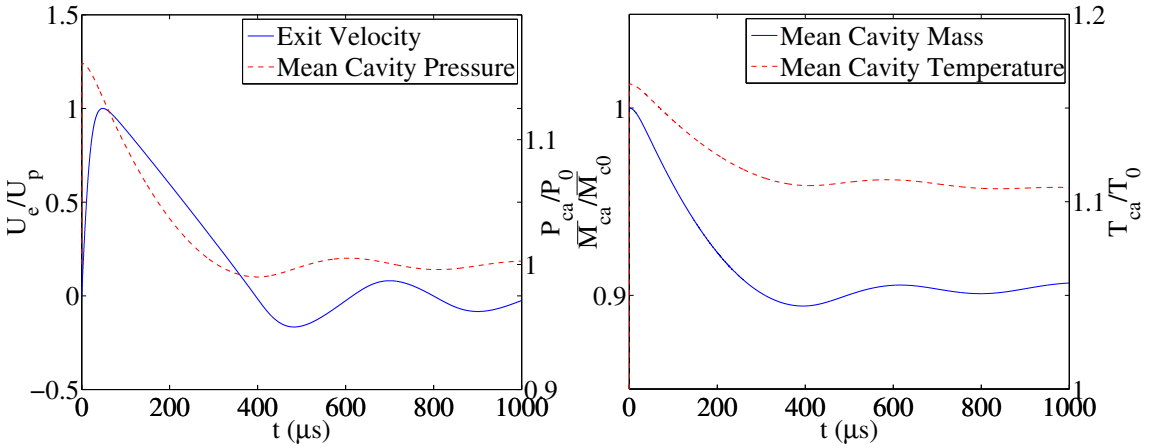

Figure 11. Temporal evolution of (**left**) jet exit velocity and mean cavity pressure; (**right**) mean cavity temperature and mass, during the start-up first cycle.

As stated before, when the discharge time reaches hundreds of microseconds, gas heating and jet expulsion would occur simultaneously. As such, Equation (13) should be used. Figure 1 shows the time evolutions of jet exit velocity and cavity pressure at a gas heating energy of $E_h = 19$ mJ and a discharge duration of 200 μs (reproduced from [28]). Initially, both the cavity pressure and the jet velocity exhibit a sharp increase. Subsequently, a plateau where the jet velocity keeps almost constant at 180 m/s is manifested and can be ascribed to the high cavity pressure sustained by continuous energy deposition. This phenomenon indicates that the jet duration time can be adjusted, not only by the total discharge energy and orifice diameter but also by the duration of energy deposition. In the later evolution, both the jet velocity and the cavity pressure oscillate periodically with a damping amplitude, meanwhile exhibiting a phase delay of approximately a quarter of the oscillation period. This phase delay is associated with the inertia of the throat gas.

The above time-response analysis applies only to the case where the actuators are working in single-shot mode and no frequency effect is present. In practice, actuators are always working repetitively at a certain frequency, and dozens of cycles are required for the actuator to reach the steady working stage. The dynamic response of the actuator to a discharge pulse in the repetitive mode largely resembles to that in the single-shot mode, nevertheless several distinctions should be noticed. As described in Section 3.1.2, in the time interval between two adjacent jet pulses, the actuator seems to behave like a Helmholtz resonator. In this case the oscillating mass is represented by the air inside the exit orifice and oscillations are caused by the stiffness of the air contained in the cavity. This occurrence has been already found during the operation of piezo-driven synthetic jet actuators, which is characterized by two natural frequencies: the membrane first-mode structural mode and the Helmholtz mode, as analysed in [5]. In the absence of mechanical moving parts, which is the case for PSJAs, only the Helmholtz natural frequency is expected (see Equation (6)).

Additionally, as all the thermodynamic variables in Equation (6) vary from cycle to cycle during the transient working stage of the actuator due to heat accumulation, the computed Helmholtz natural frequency will not stabilize until a steady stage is established. Based on the LEM model results, the typical inter-cycle variation of f_h in the transient stage is within 1–2%.

The repetitive working behaviour of the actuator was simulated by periodically depositing a fixed amount of energy (7 mJ) to the cavity at a frequency of 1 kHz [5]. Figure 12 shows the evolution of the main thermodynamic parameters over the first 25 cycles after start-up in their dimensionless form. Overall, a transient stage with asymptotic variations of all the parameters is exhibited initially and followed by a steady-state where the mass and energy equilibrium are reached. After start-up, the cavity mass globally decreases, while the cavity temperature increases monotonically, reaching as high as 800 K in the steady working stage. Note that the heat transfer effects constitute the major factor that drives suction flow, influencing the recovering rate of the cavity mass during refresh phases.

When the cavity temperature gets higher, the heat flux out of the actuator increases, resulting in an enhanced suction flow and a quick establishment of the zero-net mass flux condition.

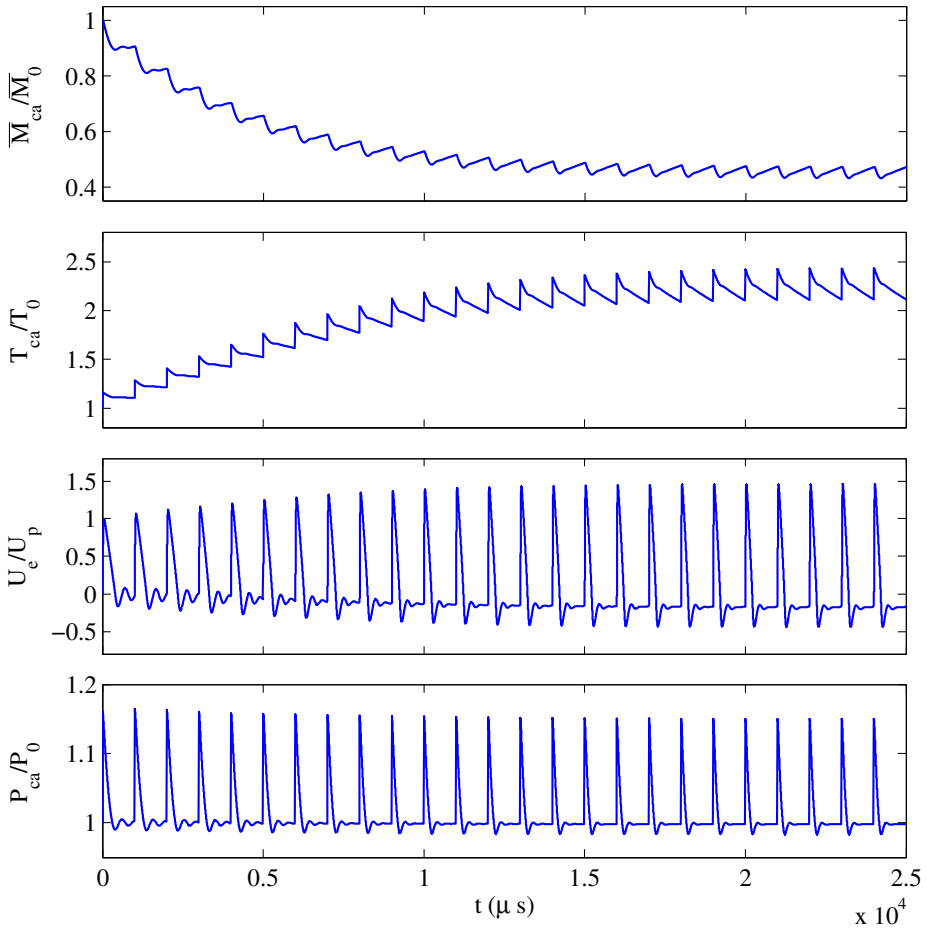

Figure 12. Evolution of the main thermo-fluid-dynamic parameters of the actuator over the first 25 cycles.

During a typical working cycle of the steady working stage, the velocity rises to a peak value of 180 m/s and oscillates around small negative values afterwards. Similarly, the cavity pressure peaks at 16 kPa and pivots around a value slightly lower than the ambient pressure in the later phases to create a steady suction flow. As interpreted earlier on, the presence of high frequency oscillations between two subsequent energy depositions is largely expected. Since the cavity density tends to decrease in the transient stage, Equation (6) predicts an increasing trend of the Helmholtz natural frequency, which to some extents can be substantiated by the last two plots in Figure 12, where the oscillation period of jet exit velocity and cavity pressure decreases slightly with the cycle number.

4. Energy Efficiency

As illustrated in Figure 4, plasma synthetic jet actuators are essentially energy conversion devices, with electrical energy and jet mechanical energy being the input and output respectively. From the perspective of energy efficiency, two questions can be posed, namely "how high the overall efficiency of the actuator is" and "how to optimize the electrical and geometrical parameters in order to maximize the overall efficiency". In fact, it can be quite confusing and striking to look at the diverse efficiency values reported in the literature (10%–35% in [27,37,38]; 1.6% in [69]; 4%–8% in [40]; 0.01%–6% in [24,28,49]). The aim of this section is to reconcile these seemingly disparate results in a unifying framework.

The energy flow in the PSJA system is illustrated by Figure 13 (reproduced from [28]). As evident, the conversion from electrical energy to mechanical energy is not straightforward, consisting of three sequential sub-processes including gas discharge, arc heating and thermodynamic cycle process [14,28,42,59]. Each of the three sub-processes exhibits inevitable energy losses, corresponding to a sub-efficiency. The overall efficiency of the actuator system ($\eta_{total} = E_m / E_{total}$) is essentially the product of these three sub-efficiencies.

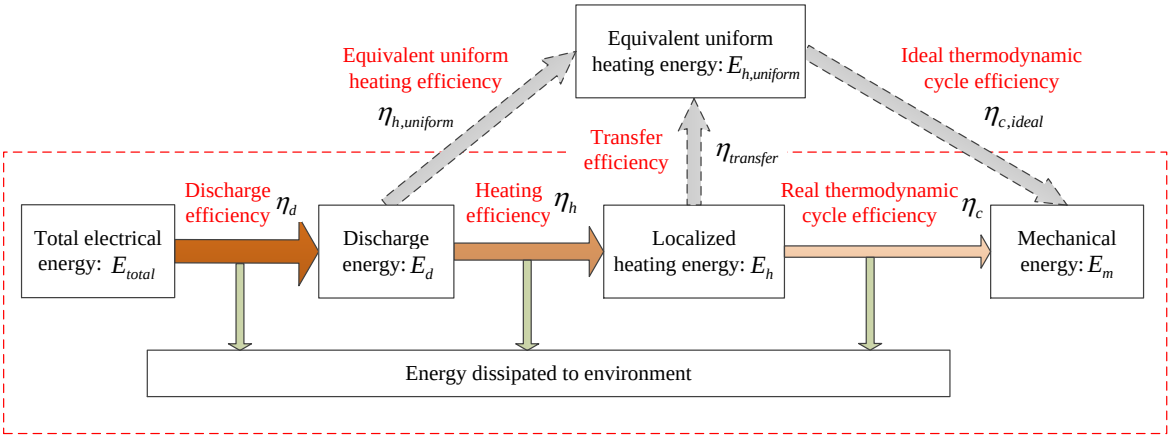

Figure 13. Energy flow in the plasma synthetic jet actuator system (reproduced from [28]). Note that the processes outside the red dash box as well as the pertinent efficiencies ($\eta_{h,\text{uniform}}$, η_{transfer} and $\eta_{c,\text{ideal}}$) are not physical.

In the following content, capacitive discharge will be taken as an example to interpret the three sub-processes. The total electrical energy refers to the capacitor energy prior to discharge ignition and can be computed as $E_{total} = C_0 U_0^2 / 2$, where C_0 and U_0 denote the capacitance and the initial voltage of the energy-storing capacitor, respectively [45]. During the gas discharge, part of the electrical energy is converted into the arc discharge energy (E_d), while the rest are consumed by the parasitic resistance of connecting wires and capacitors [14,45]. The discharge efficiency defined by $\eta_d = E_d / E_{total}$ is related to the ratio of the time-averaged arc resistance to the total parasitic resistance. As the arc resistance ($O(1\ \Omega)$) is mainly determined by the arc length and the arc temperature (proportional to plasma conductivity), the discharge efficiency decreases with increasing discharge energy, whereas increases monotonically with the electrode distance [14,30]. Typical values of η_d for capacitive discharge range from 33% to 90% [40,45,53]. In the case of pulsed DC discharge, a current-limiting resistor (O(100–1000) Ω) is usually placed in between the actuator and the DC power supply [61], leading to a much lower discharge efficiency (approximately 20% in [42]; 10%–60% in [28]), compared to a well-designed capacitive discharge circuitry.

During the arc heating process, the ionized species drift along the direction of local electrical fields and collide with neutral species. Several gas heating mechanisms are active in this process, including ion Joule heating, elastic collisions between electrons and heavy species, and vibration-to-translation relaxation of the excited heavy particles [42]. In [59], arc plasma at atmospheric condition is simulated with a magnetohydrodynamical model using the local-equilibrium assumption. Sheath loss is demonstrated to reach as high as half of the discharge energy, whereas radiation loss is typically less than 5% of the discharge energy, resulting in a gas heating efficiency (η_d) of approximately 50% for capacitive discharge. Narayanaswamy et al. [42] analysed the non-equilibrium effects in low-pressure arc plasma (35 torr) and concluded that 90% of the electrical energy is locked into the vibrationally excited heavy species (N_2 and O_2) due to the high reduced electric field ($E/N = 16$ Td), leading to a gas heating efficiency of only 10% for pulsed DC discharge. In contrast with capacitive discharge and

pulsed DC discharge, the gas heating efficiency pertaining to nanosecond-pulsed discharge is much higher (60%–77%) and increases monotonically with the slope of the voltage rising-edge [70].

In the last stage of the energy flow chart, the gas heating energy (E_h) is converted into the mechanical energy of the pulsed jets (E_m) through a thermodynamic cycle process, resulting in a cycle efficiency (η_c). As the gas inside the actuator cavity is left in a non-equilibrium state after the non-uniform arc heating, direct computation of the cycle efficiency using the pressure-volume diagram is infeasible. To solve this issue, a non-physical process is introduced which converts the non-equilibrium state left by the localized arc heating to a equivalent equilibrium state thermalized by uniform gas heating energy ($E_{h,\text{uniform}}$), under the condition that both states will produce the same amount of mechanical energy [28]. The energy conversion factor (i.e., transfer efficiency, η_{transfer}) should be less than 1 to account for the losses corresponding to shock wave propagation and reflection. The ratio of jet mechanical energy to the equivalent uniform heating energy defines the ideal thermodynamic cycle efficiency, $\eta = E_m / E_{h,\text{uniform}}$. With the energy deposition stage and the jet stage modelled as a constant-volume heating process and an isentropic expansion process respectively, $\eta_{c,\text{ideal}}$ is derived to be a simple relation of the temperature ratio during constant-volume heating process (ϵ_T), as shown in Equation (17) [28]. Consequently, $\eta_{c,\text{ideal}}$ increases monotonically with the temperature ratio.

$$\eta_{c,\text{ideal}} = 1 - \gamma \frac{\epsilon_T^{1/\gamma} - 1}{\epsilon_T - 1} \tag{17}$$

The ideal thermodynamic cycle efficiency provides an upper limit of the overall efficiency that can be achieved at a certain non-dimensional energy deposition ratio. For a typical range of $\epsilon_T < 5$ in the literature (i.e., peak jet temperature less than 1400 K, [13,34,42,55]), $\eta_{c,\text{ideal}}$ is less than 20%. Additionally, in the case that the discharge time-scale is comparable to Helmholtz natural period, the assumption of constant volume heating becomes invalid, and the energy deposition stage has to be modelled as a polytropic heating process. As a result, the ideal thermodynamic efficiency decreases with increasing discharge duration [28].

As opposed to the physical heating efficiency, the equivalent heating efficiency is much easier to access in experiments. Typically, one of the technique introduced in Section 3.1.1 is adopted to measure one of the jet intensity metrics (e.g., jet impulse [28,40], peak cavity pressure [27,38]), and the heating energy required by the actuator to yield the same jet intensity metric under assumptions of constant-volume heating and thermodynamic equilibrium is estimated by an analytical model. This estimated heating energy is essentially the equivalent uniform heating energy, and the ratio of $E_{h,\text{uniform}}$ to E_d defines the equivalent uniform heating efficiency ($\eta_{h,\text{uniform}}$). In [28], $\eta_{h,\text{uniform}}$ ranges from 10% to 35% and decreases with increasing energy deposition and cavity volume.

Up to this point, it is possible to accommodate the diverse efficiency values reported in the literature into a single framework outlined by Figure 13. The pressure-based efficiency defined by the researchers from Johns Hopkins University [27,37,38] is essentially the product of discharge efficiency and the equivalent uniform heating efficiency ($\eta_d \cdot \eta_{h,\text{uniform}}$). $\eta_d \cdot \eta_{h,\text{uniform}}$ (range: 10% to 40%) increases with electrode distance, whereas decreases with increasing energy deposition. The impulse-based efficiency determined by Golbabaei et al. [40] using a pendulum apparatus is solely the equivalent uniform heating efficiency ($\eta_{h,\text{uniform}}$). $\eta_{h,\text{uniform}}$ drops when the energy deposition goes up, whereas increases with increasing non-dimensional heating volume (the ratio of arc heating volume to cavity volume). Compared to [28], the low non-dimensional heating efficiency in [40] (4% to 8%) is attributed to the short arc length (0.8 mm, as opposed to 2 mm in [28]) and the relatively large cavity volume (234 mm^3, as opposed to 75–201 mm^3 in [28]). The electro-mechanical efficiency ($\eta_m = \eta_h \cdot \eta_c$) used in [28,49,69,71] takes the gas heating process and the thermodynamic cycle into account. η_m is on the order of O(0.1%–1%) (peak value: 6% reported by [49]), increasing monotonically with both the energy deposition and the non-dimensional heating volume. The total efficiency of PSJAs defined as $\eta_t = \eta_d \eta_h \eta_c$ are treated by [28,33], and the order of magnitudes for η_t in case of pulsed DC

discharge and capacitive discharge are $O(0.1\%)$ and $O(1\%)$ respectively, which is not striking after multiplying the three sub-efficiencies together (η_d: 10%–90%; η_h: 4%–40%; η_c: <20%).

5. Flow Control Applications

Owing to the unique feature of producing high-velocity (>300 m/s) pulsed jets at high frequency (>5 kHz), applications of PSJAs can be found widely from moderate- to high-Reynolds-number flows including flow separation control in airfoils/ramps [72], jet noise control [12], shock wave/boundary layer interaction control [18] and so on. A classification of these application studies based on the research groups that were involved is shown in Table 2.

Table 2. Institutions involved in the application studies of plasma synthetic jet actuators. ONERA–The French Aerospace Lab; UNINA–The University of Naples Federico II; UT Austin–The University of Texas at Austin; AFEU–Air Force Engineering University; NUDT–National University of Defense Technology.

Category	Institutions	Representative Literatures
Separation control at moderate-Reynolds number	ONERA; Xiamen University; UNINA	[35,72,73]
Jet noise control	ONERA	[12,74,75]
Shock wave/boundary layer interaction control	UT Austin; AFEU; NUDT	[18,76–83]

In separation control cases, PSJs are typically issued upstream of the separation region, either in the wall-normal direction to create a quasi-streamwise counter-rotating vortex pair [84] or pitched and skewed with respect to the main flow to produce a single dominant streamwise vortex [12]. These vortices transport the high-momentum flow from the outer boundary layer to the near-wall region, resulting in a fuller boundary layer velocity profile and a reduction in boundary layer shape factor (1.3–1.2 in [84]). In [72], 5 actuators arranged in two rows with 30° pitching angle and 60° skew angle are embedded in the plateau upstream of a decelerating ramp to eliminate the separated flow. At a freestream velocity of 37 m/s (ramp-height based Reynolds number: 6.2×10^4), the area of the separation region decreases significantly with the increasing actuation frequency at $f_d < 500$ Hz whereas remains unchanged afterwards. Additionally, Caruana et al. [72] used an array of 20 actuators to control the trailing-edge separation over an NACA-0015 airfoil model. The actuators are placed 32% chord length (c) away from the leading edge, and the same pitch and skew angle are used as in the ramp experiment. At a freestream velocity of 40 m/s (chord-based Reynolds number: $Re_c = 1.2 \times 10^6$) and an angle of attack of 11.5°, the separation region initially occupying half of the chord shrinks monotonically when the actuation frequency increases, and a fully attached flow is obtained at $f_d > 250$ Hz. In [73], three PSJAs are employed to control the flow separation over an NACA 0021 wing model at $U_\infty = 20$ m/s and $Re_c = 3.4 \times 10^5$. Different actuation locations ($0.15c$ and $0.45c$) and jet pitching angles (45° and 60°) are examined. As a result, PSJs issued at 15% chord length is able to postpone the stall angle by 2° and increase the peak lift coefficient by 9%. The two jet pitching angles show similar control effects. Arena et al. [35] concerned the potential interferences (electrical and thermal) between PSJAs and other electronic devices hosted by the morphing flap in practical terms, and concluded that appropriate shielding is necessary to reduce the electromagnetic field produced by the actuators to a level that is compatible with other electronic devices.

For the purposes of jet noise control, the actuators are generally accommodated in the nozzle lip to seed disturbances in the jet shear layer. As a result of Kelvin–Helmholtz instability, these disturbances are expected to grow into large-scale structures and change the overall sound level emitted by jets [12]. In [74], 12 actuators are distributed evenly around the lip of a 50 mm diameter nozzle, and an exit Mach number of 0.6 is tested (exit-diameter based Reynolds number: 7×10^5). For an actuation

Strouhal number close to 0.3, the jet noise is increased by 3–4 dB. A slight noise decrease of -0.3 dB is demonstrated when the neighbouring actuators are operated 180° out of phase. Chedevergne et al. [75] performed numerical simulation on the same jet flow tested by [74]. Only one actuator is modelled and a hybrid RANS-LES approach is adopted, to save the computation resources. Based on their results, the pressure waves created by the arc discharge are responsible for the development of the large-scale structures observed in the jet mixing layer, whereas the pulsed jets play a secondary role.

In earlier studies of PSJAs at supersonic flow, jets are ejected in the wall-normal direction to impinge the crossflow boundary layer, and the penetration authority is quantified either by the deflection angles of the induced shock waves or by the trajectories of the detected jet front. In [42], a jet penetration distance of 1.5 boundary layer thickness (6 mm) is measured in a Mach 3 crossflow using Schlieren imaging, and the jet-to-crossflow momentum flux ratio is estimated to be 0.6 at $\epsilon \approx 35$. Emerick et al. [43,50] employed an array of three PSJAs to interact with a Mach 1.5 crossflows, and a maximum flow deflection angle of 5° is obtained in single-shot mode at $\epsilon \approx 40$. This angle is equivalent to that created by a steady microjet at a pressure ratio of 3.2. Zhou et al. [83] performed a similar test in a Mach 2 crossflow, and the jet-to-crossflow momentum flux ratios determined from matching the measured jet trajectories with the empirical relations ranges from 0.6 to 1.3 with increasing non-dimensional energy deposition of 75–205.

Recent studies of PSJAs at supersonic flow show consistent interests in shock wave boundary layer interaction (SWBLI) control. The objectives of SWBLI control include two aspects: one to reduce the massive flow separation induced by the steep pressure rise, the other to shift/mitigate the low-frequency unsteadiness related to the separated flow [85]. UT Austin has shown pioneering results in SWBLI control with PSJAs. In [18,77], an array of plasma jets pitched at 45° and skewed at 90° were positioned approximately 4 times of the boundary layer thickness (δ) upstream of the separation shock, to control the SWBLI induced by a ramp model in a Mach 3 crossflow. The transient response of the shock systems was diagnosed with high-speed Schlieren imaging, phase-locked laser scattering imaging and wall pressure measurements [86]. Results show that the separation shock executes a small initial downstream displacement of $\delta/4$ for a time period of 5–10 μs, followed by a large upstream displacement of about 1δ. The dominant frequency of the separation shock motion is shifted to the discharge frequency. When PSJs are pulsed at an interaction-length based Strouhal number of $St_L = 0.04$, the overall magnitude of the pressure fluctuations associated with the unsteady large-scale motion of the separated flow is decreased by 30%. With higher pulsing frequency ($St_L = 0.66$), the oscillation amplitude of the separation shock is reduced to less than half of the boundary layer thickness. As a follow-up and complement of the above-mentioned works, Greene et al. [78] performed a parametric study on the major factors that influencing the mean separation length induced by a 20° ramp. Surface oil streak visualizations showed that PSJA are able to reduce the distance between the separation line and the compression corner by 40%. The optimum jet placement proves to be 1.5δ upstream of the compression corner, beyond which the effect of the jets diminishes. The optimum jet configuration is a combination of low pitch angle and zero skew angle.

In [81], a row of five PSJAs arranged in the spanwise direction was used to control the SWBLI induced by a 30° ramp in a Mach 2 flow. The size of the separation zone was reduced during the interaction with the jet plume, meanwhile an upstream motion of both the separation and the reattachment shock was observed. The control effect improves while the discharge energy and the orifice diameter increase, which is consistent with that in [83]. In [79,80], different configurations of the actuator array (i.e., spanwise, streamwise) were considered, and a longer modification of the shock wave system is demonstrated when actuators are arranged in the streamwise direction and triggered simultaneously. Yang et al. [87] numerically investigated the control mechanism of SWBLI and concluded that the jet plume acts as a virtual micro vortex generator, which promotes the mixing within the turbulent boundary layer and enhances its ability to resist flow separation.

6. Conclusions and Recommendations

Since the introduction of the "sparkjet" concept by Grossman et al. in 2003 [6], considerable efforts have been made to characterize the performance of PSJAs in quiescent condition, using experimental, analytical and numerical methodologies. So far, the majority of the parameters that potentially affect the actuator performance have been identified and further classified into three categories, i.e., electrical, geometrical and atmospheric. These parameters were combined as non-dimensional metrics (e.g., non-dimensional energy deposition, dimensionless frequency, non-dimensional heating volume) to generalize/collapse the trends observed at different operation conditions. The peak jet velocity produced by a specific actuator scales approximately with the cubic root of the non-dimensional energy deposition, while the limit working frequency of the actuator is defined by the Helmholtz natural resonance frequency of the actuator cavity, which can be tuned by the cavity volume, exit orifice area and exit nozzle length. The total efficiency of the actuator, depending on the discharge waveforms, actuator geometry and atmospheric parameters, ranges from 0.01% to 1%.

Based on these generalized trends, it is possible to "optimally" (in an efficiency-oriented way) design a PSJA that meets certain performance metrics including frequency response, peak velocity, and momentum flux, with minimum trial and error. These performance metrics are generally derived from the characteristics scales of the target flow, using Strouhal number, velocity ratio, momentum coefficient and so on. Notwithstanding how charming this design process could be, the unknown total efficiency imposes considerable uncertainties while trying to project the jet intensity metrics back to the input electric parameters. As such, future parametric studies on the formation process of PSJs are recommended to give indications of the energy loss mechanisms inside the actuator cavities (e.g., gas ionization, heat conduction, radiation), in order to improve the predication accuracy of the total and sub- efficiency. Particularly, a deep understanding of the plasma heating physics for various gas discharges is necessitated, and an empirical model of the arc heating efficiency that can be applied to a wide range of operating conditions (i.e., discharge energy, discharge type), is highly demanded.

Pivoting around a higher actuator efficiency, several cross-validated observations can already be used as the optimization criteria for actuator geometry as well as discharge circuit design. Specifically, pulsed-DC discharge using a current-limit resistor is not recommended due to the low discharge efficiency. The parasitic resistance of the electrical components including inductors and connecting wires shall be minimized to increase the discharge efficiency. Within the breakdown ability of the trigger discharge, the electrode distance shall be extended to increase the arc heating volume; For the same arc size and discharge energy, a small cavity volume is preferred to increase the heating temperature ratio. Once the structure requirements are met, the throat length of the actuator shall be minimized to increase the Helmholtz natural frequency.

Compared to the characterization studies (typically conducted in quiescent flow conditions), PSJA-based flow control application has progressed relatively slower and only a few investigations have been performed up to date. Nevertheless, these limited investigations are already sufficient to demonstrate the authority of PSJs in manipulating high-speed, high-Reynolds-number flow. In the case of separation control where a fuller boundary layer velocity profile is desired (e.g., airfoil trailing edge separation, SWBLI, ramp flow separation), the actuator is typically operated in the "vortex generator jet" mode, with skewed and pitched jets ejected upstream of the separation region, in order to create quasi-streamwise vortices that enhance the mixing in the boundary layer. For jet noise control, Kelvin–Helmholtz instability in the jet shear layer can be leveraged to amplify the disturbances seeded by the actuator into large-scale vortex structures, thus modifying the far-field acoustics. In this process, the pressure waves induced by the pulsed arc discharge play a dominant role over the pulsed jets.

The slow progress of application studies can be ascribed to several aspects. Apart from the inherent difficulties of performing numerical simulations/measurements in high-speed high-Reynolds-number flow, the complexity of designing a reliable discharge circuit that can feed multiple actuators at high repetition rate, as well as the overwhelming EMI incurred by rapid arc discharges which frequently disrupts the measurement chain (PIV, hot-wire, dynamic pressure

transducers), also play a role. In future studies, these technical issues should be noticed, and the compatibility of PSJAs with the surrounding equipment/environment in terms of acoustic emission, EMI, and thermal management, has to be evaluated. Detailed parametric studies shall be carried out to extract the optimal actuation parameters (e.g., jet orientation, velocity ratio, Strouhal number) and the corresponding control mechanisms at different target flows including SWBLI, shock buffet control, high-Reynolds number airfoil separation control and so on. The relation between actuator input parameters and flow control effectiveness metrics is recommended to be displayed in the non-dimensional form to facilitate easy comparison between different studies, as well as to generalize the observed trends. Most importantly, it has to be evaluated whether the benefits returned by the target flow can well cover the power/weight penalties incurred by implementing the active flow control system. For drag reduction cases, a preferable evaluation parameter is the power saving ratio, which considers the relative weight between the power saved by drag reduction and the electrical power used to feed the actuators.

Author Contributions: Conceptualization, L.d.L.; Writing—original draft preparation, H.Z. and M.C.; Writing—review and editing, H.Z., M.K., and M.C.; Supervison, M.K. and L.d.L.

Conflicts of Interest: The authors declare no conflict of interest.

References

1. Cattafesta, L.N., III; Sheplak, M. Actuators for active flow control. *Annu. Rev. Fluid Mech.* **2011**, *43*, 247–272. [CrossRef]
2. Gad-el Hak, M. *Flow Control: Passive, Active, and Reactive Flow Management*, 1st ed.; Cambridge University Press: Cambridge, UK, 2000.
3. Joslin, R.D.; Miller, D.N. (Eds.) *Fundamentals and Applications of Modern Flow Control*; American Institute of Aeronautics and Astronautics: Reston, VA, USA, 2009.
4. Glezer, A.; Amitay, M. Synthetic jets. *Annu. Rev. Fluid Mech.* **2002**, *34*, 503–529. [CrossRef]
5. Chiatto, M.; Capuano, F.; Coppola, G.; de Luca, L. LEM characterization of synthetic jet actuators driven by piezoelectric element: A review. *Sensors* **2017**, *17*, 1216. [CrossRef] [PubMed]
6. Grossman, K.; Bohdan, C.; VanWie, D. Sparkjet actuators for flow control. In Proceedings of the 41st Aerospace Sciences Meeting and Exhibit, Reno, NV, USA, 6–9 January 2003; p. 57.
7. Cybyk, B.; Grossman, K.; Wilkerson, J. Performance characteristics of the sparkjet flow control actuator. In Proceedings of the 2nd AIAA Flow Control Conference, Portland, OR, USA, 28 June–1 July 2004; p. 2131.
8. Cybyk, B.; Grossman, K.; Wilkerson, J.; Chen, J.; Katz, J. Single-pulse performance of the sparkjet flow control actuator. In Proceedings of the 43rd AIAA Aerospace Sciences Meeting and Exhibit, Reno, NV, USA, 10–13 January 2005; p. 401.
9. Cybyk, B.; Land, H.; Simon, D.; Chen, J.; Katz, J. Experimental characterization of a supersonic flow control actuator. In Proceedings of the 44th AIAA Aerospace Sciences Meeting and Exhibit, Reno, NV, USA, 9–12 January 2006; p. 478.
10. Haack Popkin, S.; Cybyk, B.; Land, B.; Foster, C.; Emerick, T.; Alvi, F. Recent Performance-Based Advances in SparkJet Actuator Design for Supersonic Flow Applications. In Proceedings of the 51st AIAA Aerospace Sciences Meeting including the New Horizons Forum and Aerospace Exposition, Grapevine, TX, USA, 7–10 January 2013; p. 322.
11. Caruana, D.; Barricau, P.; Hardy, P. The "Plasma Synthetic Jet" Actuator. Aero-thermodynamic Characterization and First Flow Control Applications. In Proceedings of the 47th AIAA Aerospace Sciences Meeting including the New Horizons Forum and Aerospace Exposition, Orlando, FL, USA, 5–8 January 2009; p. 1307.
12. Hardy, P.; Barricau, P.; Caruana, D.; Gleyzes, C.; Belinger, A.; Cambronne, J.P. Plasma synthetic jet for flow control. In Proceedings of the 40th Fluid Dynamics Conference and Exhibit, Chicago, IL, USA, 28 June–1 July 2010; p. 5103.
13. Belinger, A.; Hardy, P.; Barricau, P.; Cambronne, J.; Caruana, D. Influence of the energy dissipation rate in the discharge of a plasma synthetic jet actuator. *J. Phys. D Appl. Phys.* **2011**, *44*, 365201. [CrossRef]

14. Belinger, A.; Naudé, N.; Cambronne, J.; Caruana, D. Plasma synthetic jet actuator: Electrical and optical analysis of the discharge. *J. Phys. D Appl. Phys.* **2014**, *47*, 345202. [CrossRef]
15. Dufour, G.; Hardy, P.; Quint, G.; Rogier, F. Physics and models for plasma synthetic jets. *Int. J. Aerodyn.* **2013**, *3*, 47–70. [CrossRef]
16. Sary, G.; Dufour, G.; Rogier, F.; Kourtzanidis, K. Modeling and parametric study of a plasma synthetic jet for flow control. *AIAA J.* **2014**, *52*, 1591–1603. [CrossRef]
17. Narayanaswamy, V.; Shin, J.; Clemens, N.; Raja, L. Investigation of plasma-generated jets for supersonic flow control. In Proceedings of the 46th AIAA Aerospace Sciences Meeting and Exhibit, Reno, NV, USA, 7–10 January 2008; p. 285.
18. Narayanaswamy, V.; Raja, L.L.; Clemens, N.T. Control of a shock/boundary-layer interaction by using a pulsed-plasma jet actuator. *AIAA J.* **2012**, *50*, 246–249. [CrossRef]
19. Reedy, T.M.; Kale, N.V.; Dutton, J.C.; Elliott, G.S. Experimental characterization of a pulsed plasma jet. *AIAA J.* **2013**, *51*, 2027–2031. [CrossRef]
20. Anderson, K.V.; Knight, D.D. Plasma jet for flight control. *AIAA J.* **2012**, *50*, 1855–1872. [CrossRef]
21. Zong, H.; Wu, Y.; Jia, M.; Song, H.; Liang, H.; Li, Y.; Zhang, Z. Influence of geometrical parameters on performance of plasma synthetic jet actuator. *J. Phys. D Appl. Phys.* **2015**, *49*, 025504. [CrossRef]
22. Zong, H.; Kotsonis, M. Characterisation of plasma synthetic jet actuators in quiescent flow. *J. Phys. D Appl. Phys.* **2016**, *49*, 335202. [CrossRef]
23. Chiatto, M.; de Luca, L. Numerical and Experimental Frequency Response of Plasma Synthetic Jet Actuators. In Proceedings of the 55th AIAA Aerospace Sciences Meeting, Grapevine, TX, USA, 9–13 January 2017. [CrossRef]
24. Zong, H.; Kotsonis, M. Electro-mechanical efficiency of plasma synthetic jet actuator driven by capacitive discharge. *J. Phys. D Appl. Phys.* **2016**, *49*, 455201. [CrossRef]
25. Zong, H.; Cui, W.; Wu, Y.; Zhang, Z.; Liang, H.; Jia, M.; Li, Y. Influence of capacitor energy on performance of a three-electrode plasma synthetic jet actuator. *Sens. Actuators A Phys.* **2015**, *222*, 114–121. [CrossRef]
26. Zhang, Z.; Wu, Y.; Jia, M.; Zong, H.; Cui, W.; Liang, H.; Li, Y. Influence of the discharge location on the performance of a three-electrode plasma synthetic jet actuator. *Sens. Actuators A Phys.* **2015**, *235*, 71–79. [CrossRef]
27. Popkin, S.H.; Cybyk, B.Z.; Foster, C.H.; Alvi, F.S. Experimental estimation of SparkJet efficiency. *AIAA J.* **2016**, *54*, 1831–1845. [CrossRef]
28. Zong, H.; Wu, Y.; Song, H.; Jia, M. Efficiency characteristic of plasma synthetic jet actuator driven by pulsed direct-current discharge. *AIAA J.* **2016**, *54*, 3409–3420. [CrossRef]
29. Roth, J. *Industrial Plasma Engineering. Volume 1: Principles*; Institute of Physics Publishing: Bristol, UK; Philadelphia, PA, USA, 1995.
30. Popkin, S.H.; Taylor, T.M.; Cybyk, B.Z. Development and application of the sparkjet actuator for high-speed flow control. *Johns Hopkins APL Tech. Dig.* **2013**, *32*, 404–418.
31. Chiatto, M.; Palumbo, A.; de Luca, L. A Calibrated Lumped Element Model for the Prediction of PSJ Actuator Efficiency Performance. *Actuators* **2018**, *7*, 10. [CrossRef]
32. Haack, S.; Land, H.; Cybyk, B.; Ko, H.; Katz, J. Characterization of a high-speed flow control actuator using digital speckle tomography and PIV. In Proceedings of the 4th AIAA Flow Control Conference, Seattle, WA, USA, 23–26 June 2008.
33. Zong, H.; Kotsonis, M. Formation, evolution and scaling of plasma synthetic jets. *J. Fluid Mech.* **2018**, *837*, 147–181. [CrossRef]
34. Zong, H.; Wu, Y.; Li, Y.; Song, H.; Zhang, Z.; Jia, M. Analytic model and frequency characteristics of plasma synthetic jet actuator. *Phys. Fluids* **2015**, *27*, 027105. [CrossRef]
35. Arena, M.; Chiatto, M.; Amoroso, F.; Pecora, R.; de Luca, L. Feasibility studies for the installation of Plasma Synthetic Jet Actuators on the skin of a morphing wing flap. *Proc. SPIE* **2018**, *10595*, 105950M. [CrossRef]
36. Tang, M.; Wu, Y.; Wang, H.; Jin, D.; Guo, S.; Gan, T. Effects of Capacitance on a Plasma Synthetic jet Actuator with a conical cavity. *Sens. Actuators A Phys.* **2018**, *276*, 284–295. [CrossRef]
37. Haack, S.; Taylor, T.; Emhoff, J.; Cybyk, B. Development of an analytical SparkJet model. In Proceedings of the 5th Flow Control Conference, Chicago, IL, USA, 28 June–1 July 2010; p. 4979.

38. Haack, S.; Taylor, T.; Cybyk, B.; Foster, C.; Alvi, F. Experimental estimation of sparkjet efficiency. In Proceedings of the 42nd AIAA Plasmadynamics and Lasers Conference in Conjunction with the 18th International Conference on MHD Energy Conversion (ICMHD), Honolulu, HI, USA, 27–30 June 2011; p. 3997.
39. Wang, L.; Xia, Z.x.; Luo, Z.b.; Chen, J. Three-electrode plasma synthetic jet actuator for high-speed flow control. *AIAA J.* **2013**, *52*, 879–882. [CrossRef]
40. Golbabaei-Asl, M.; Knight, D.; Wilkinson, S. Novel technique to determine sparkjet efficiency. *AIAA J.* **2014**, *53*, 501–504. [CrossRef]
41. Jin, D.; Cui, W.; Li, Y.; Li, F.; Jia, M.; Sun, Q.; Zhang, B. Characteristics of pulsed plasma synthetic jet and its control effect on supersonic flow. *Chin. J. Aeronaut.* **2015**, *28*, 66–76. [CrossRef]
42. Narayanaswamy, V.; Raja, L.L.; Clemens, N.T. Characterization of a high-frequency pulsed-plasma jet actuator for supersonic flow control. *AIAA J.* **2010**, *48*, 297–305. [CrossRef]
43. Emerick, T.; Ali, M.; Foster, C.; Alvi, F.; Haack Popkin, S.; Cybyk, B. Sparkjet actuator characterization in supersonic crossflow. In Proceedings of the 6th AIAA Flow Control Conference, New Orleans, LA, USA, 25–28 June 2012; p. 2814.
44. Jin, D.; Li, Y.; Jia, M.; Song, H.; Cui, W.; Sun, Q.; Li, F. Experimental characterization of the plasma synthetic jet actuator. *Plasma Sci. Technol.* **2013**, *15*, 1034–1040. [CrossRef]
45. Wang, L.; Xia, Z.; Luo, Z.; Zhang, Y. Effect of pressure on the performance of plasma synthetic jet actuator. *Sci. China Phys. Mech. Astron.* **2014**, *57*, 2309–2315. [CrossRef]
46. Zong, H.; Kotsonis, M. Experimental investigation on frequency characteristics of plasma synthetic jets. *Phys. Fluids* **2017**, *29*, 115107. [CrossRef]
47. Grossman, K.; Cybyk, B.; VanWie, D.; Rigling, M. Characterization of sparkjet actuators for flow control. In Proceedings of the 42nd AIAA Aerospace Sciences Meeting and Exhibit, Reno, NV, USA, 5–8 January 2004; p. 89.
48. Wang, L.; Xia, Z.; Luo, Z.; Zhou, Y.; Zhang, Y. Experimental study on the characteristics of a two-electrode plasma synthetic jet actuator. *Acta Phys. Sin.* **2014**, *63*, 194702.
49. Zong, H. Influence of Nondimensional Heating Volume on Efficiency of Plasma Synthetic Jet Actuators. *AIAA J.* **2017**, *56*, 1–4. [CrossRef]
50. Emerick, T.; Ali, M.; Foster, C.; Alvi, F.; Popkin, S. SparkJet characterizations in quiescent and supersonic flowfields. *Exp. Fluids* **2014**, *55*, 1858. [CrossRef]
51. Zhang, Z.; Wu, Y.; Jia, M.; Song, H.; Sun, Z.; Zong, H.; Li, Y. The multichannel discharge plasma synthetic jet actuator. *Sens. Actuators A Phys.* **2017**, *253*, 112–117. [CrossRef]
52. Zong, H.; Kotsonis, M. Effect of slotted exit orifice on performance of plasma synthetic jet actuator. *Exp. Fluids* **2017**, *58*, 17. [CrossRef]
53. Li, Y.; Jia, M.; Wu, Y.; Li, Y.H.; Zong, H.H.; Song, H.M.; Liang, H. Influence of air pressure on the performance of plasma synthetic jet actuator. *Chin. Phys. B* **2016**, *25*, 095205. [CrossRef]
54. Zong, H.; Wu, Y.; Song, H.; Jia, M.; Liang, H.; Li, Y.; Zhang, Z. Investigation of the performance characteristics of a plasma synthetic jet actuator based on a quantitative Schlieren method. *Meas. Sci. Technol.* **2016**, *27*, 055301. [CrossRef]
55. Ko, H.; Haack, S.; Land, H.; Cybyk, B.; Katz, J.; Kim, H. Analysis of flow distribution from high-speed flow actuator using particle image velocimetry and digital speckle tomography. *Flow Meas. Instrum.* **2010**, *21*, 443–453. [CrossRef]
56. Gil, P.; Strzelczyk, P. Performance and efficiency of loudspeaker driven synthetic jet actuator. *Exp. Therm. Fluid Sci.* **2016**, *76*, 163–174. [CrossRef]
57. Trávníček, Z.; Kordík, J. Energetic efficiencies of synthetic jet actuators: Commentary on the article by Gil and Strzelczyk. *Exp. Therm. Fluid Sci.* **2018**, *98*, 121–123. [CrossRef]
58. Cybyk, B.; Grossman, K.; Van Wie, D. Computational assessment of the sparkjet flow control actuator. In Proceedings of the 33rd AIAA Fluid Dynamics Conference and Exhibit, Orlando, FL, USA, 23–26 June 2003; p. 3711.
59. Zhang, Z.; Wu, Y.; Jia, M.; Song, H.; Sun, Z.; Li, Y. MHD-RLC discharge model and the efficiency characteristics of plasma synthetic jet actuator. *Sens. Actuators A Phys.* **2017**, *261*, 75–84. [CrossRef]
60. Smy, P.; Clements, R.; Dale, J.; Simeoni, D.; Topham, D. Efficiency and erosion characteristics of plasma jet igniters. *J. Phys. D Appl. Phys.* **1983**, *16*, 783. [CrossRef]

61. Shin, J. Characteristics of high speed electro-thermal jet activated by pulsed DC discharge. *Chin. J. Aeronaut.* **2010**, *23*, 518–522. [CrossRef]
62. Gharib, M.; Rambod, E.; Shariff, K. A universal time scale for vortex ring formation. *J. Fluid Mech.* **1998**, *360*, 121–140. [CrossRef]
63. Laurendeau, F.; Chedevergne, F.; Casalis, G. Transient ejection phase modeling of a plasma synthetic jet actuator. *Phys. Fluids* **2014**, *26*, 125101. [CrossRef]
64. Gutmark, E.; Grinstein, F. Flow control with noncircular jets. *Annu. Rev. Fluid Mech.* **1999**, *31*, 239–272. [CrossRef]
65. Quint, G.; Rogier, F.; Dufour, G. Numerical modelling of the electrical arc created inside the cavity of the PSJ actuator. In Proceedings of the 20th AIAA Computational Fluid Dynamics Conference, Honolulu, HI, USA, 27–30 June 2011.
66. Laurendeau, F.; Léon, O.; Chedevergne, F.; Senoner, J.M.; Casalis, G. Particle image velocimetry experiment analysis using large-eddy simulation: Application to plasma actuators. *AIAA J.* **2017**, *55*, 3767–3780. [CrossRef]
67. Capitelli, M.; Colonna, G.; Gorse, C.; D'Angola, A. Transport properties of high temperature air in local thermodynamic equilibrium. *Eur. Phys. J. D* **2010**, *11*, 279–289. [CrossRef]
68. de Luca, L.; Girfoglio, M.; Chiatto, M.; Coppola, G. Scaling properties of resonant cavities driven by piezo-electric actuators. *Sens. Actuators A Phys.* **2016**, *247*, 465–474. [CrossRef]
69. Wang, L.; Luo, Z.B.; Xia, Z.X.; Liu, B. Energy efficiency and performance characteristics of plasma synthetic jet. *Acta Phys. Sin.* **2013**, *62*, 125207. [CrossRef]
70. Zhu, Y.; Wu, Y.; Jia, M.; Liang, H.; Li, J.; Li, Y. Influence of positive slopes on ultrafast heating in an atmospheric nanosecond-pulsed plasma synthetic jet. *Plasma Sources Sci. Technol.* **2014**, *24*, 015007. [CrossRef]
71. Zong, H.; Kotsonis, M. Realisation of plasma synthetic jet array with a novel sequential discharge. *Sens. Actuators A Phys.* **2017**, *266*, 314–317. [CrossRef]
72. Caruana, D.; Rogier, F.; Dufour, G.; Gleyzes, C. The plasma synthetic jet actuator, physics, modeling and flow control application on separation. *AerospaceLab* **2013**, *6*, 1.
73. Liu, R.; Niu, Z.; Wang, M.; Hao, M.; Lin, Q. Aerodynamic control of NACA 0021 airfoil model with spark discharge plasma synthetic jets. *Sci. China Technol. Sci.* **2015**, *58*, 1949–1955. [CrossRef]
74. Léon, O.; Caruana, D.; Castelain, T. Increase and decrease of the noise radiated by high-Reynolds-number subsonic jets through plasma synthetic jet actuation. In Proceedings of the International Conference on Acoustic Climate Inside and Outside Buildings, Vilnius, Lithuania, 23–26 September 2014.
75. Chedevergne, F.; Léon, O.; Bodoc, V.; Caruana, D. Experimental and numerical response of a high-Reynolds-number M = 0.6 jet to a Plasma Synthetic Jet actuator. *Int. J. Heat Fluid Flow* **2015**, *56*, 1–15. [CrossRef]
76. Narayanaswamy, V. Investigation of a Pulsed-Plasma Jet for Separation Shock/boundary Layer Interaction Control. Ph.D. Thesis, The University of Texas at Austin, Austin, TX, USA, 2010.
77. Narayanaswamy, V.; Raja, L.L.; Clemens, N.T. Control of unsteadiness of a shock wave/turbulent boundary layer interaction by using a pulsed-plasma-jet actuator. *Phys. Fluids* **2012**, *24*, 076101. [CrossRef]
78. Greene, B.; Clemens, N.; Magari, P.; Micka, D. Control of mean separation in shock boundary layer interaction using pulsed plasma jets. *Shock Waves* **2015**, *25*, 495–505. [CrossRef]
79. Jin, D.; Jia, M.; Song, H.; Wu, Y.; Li, F. Control Effect of Arc-driven Plasma Synthetic Jet on Supersonic Shockwave. In Proceedings of the 21st AIAA International Space Planes and Hypersonics Technologies Conference, Xiamen, China, 6–9 March 2017; p. 2228.
80. Wang, H.; Li, J.; Jin, D.; Dai, H.; Gan, T.; Wu, Y. Effect of a transverse plasma jet on a shock wave induced by a ramp. *Chin. J. Aeronaut.* **2017**, *30*, 1854–1865. [CrossRef]
81. Wang, H.; Li, J.; Jin, D.; Zhang, Z.; Tang, M.; Wu, Y. Manipulation of ramp-induced shock wave/boundary layer interaction using a transverse plasma jet array. *Int. J. Heat Fluid Flow* **2017**, *67*, 133–137.
82. Wang, H.; Li, J.; Jin, D.; Tang, M.; Wu, Y.; Xiao, L. High-frequency counter-flow plasma synthetic jet actuator and its application in suppression of supersonic flow separation. *Acta Astronaut.* **2018**, *142*, 45–56. [CrossRef]
83. Zhou, Y.; Xia, Z.; Luo, Z.; Wang, L. Effect of three-electrode plasma synthetic jet actuator on shock wave control. *Sci. China Technol. Sci.* **2017**, *60*, 146–152. [CrossRef]
84. Zong, H.; Kotsonis, M. Interaction between plasma synthetic jet and subsonic turbulent boundary layer. *Phys. Fluids* **2017**, *29*, 045104. [CrossRef]

85. Babinsky, H.; Harvey, J.K. *Shock Wave-Boundary-Layer Interactions*; Cambridge University Press: Cambridge, UK, 2011; Volume 32.
86. Narayanaswamy, V.; Clemens, N.T.; Raja, L.L. Method for acquiring pressure measurements in presence of plasma-induced interference for supersonic flow control applications. *Meas. Sci. Technol.* **2011**, *22*, 125107. [CrossRef]
87. Yang, G.; Yao, Y.; Fang, J.; Gan, T.; Lu, L. Large-eddy simulation of shock-induced flow separation control using SparkJet concept. In Proceedings of the 54th AIAA Aerospace Sciences Meeting, San Diego, CA, USA, 4–8 January 2016; p. 0045.